Hydrogen fluoride total and partial column time series above the Jungfraujoch from long-term FTIR measurements: Impact of the line-shape model, characterization of the error budget and seasonal cycle, and comparison with satellite and model data

P. Duchatelet,[1] P. Demoulin,[1] F. Hase,[2] R. Ruhnke,[2] W. Feng,[3] M. P. Chipperfield,[3] P. F. Bernath,[4] C. D. Boone,[5] K. A. Walker,[5,6] and E. Mahieu[1]

[1] Time series of hydrogen fluoride (HF) total columns have been derived from ground-based Fourier transform infrared (FTIR) solar spectra recorded between March 1984 and December 2009 at the International Scientific Station of the Jungfraujoch (Swiss Alps, 46.5°N, 8.0°E, 3580 m asl) with two high-resolution spectrometers (one homemade and one Bruker 120-HR). Solar spectra have been inverted with the PROFFIT 9.5 algorithm, using the optimal estimation method. An intercomparison of HF total columns retrieved with PROFFIT and SFIT-2–the other reference algorithm in the FTIR community–is performed for the first time. The effect of a Galatry line shape model on HF retrieved total columns and vertical profiles, on the residuals of the fits and on the error budget is also quantified. Information content analysis indicates that in addition to HF total vertical abundance, three independent stratospheric HF partial columns can be derived from our Bruker spectra. A complete error budget has been established and indicates that the main source of systematic error is linked to HF spectroscopy and that the random error affecting our HF total columns does not exceed 2.5%. Ground-based middle and upper stratospheric HF amounts have been compared to satellite data collected by the HALOE or ACE-FTS instruments. Comparisons of our FTIR HF total and partial columns with runs performed by two three-dimensional numerical models (SLIMCAT and KASIMA) are also included. Finally, FTIR and model HF total and partial columns time series have been analyzed to derive the main characteristics of their seasonal cycles.

1. Introduction

[2] Fluorine enters the stratosphere mainly in the form of chlorofluorcarbons (CFCs) and hydrochlorofluorocarbons (HCFCs) which have been widely emitted at ground level by human activities over the past few decades. Among these man-made components, primary contributors to atmospheric fluorine are CFC-11 (CCl_3F) and CFC-12 (CCl_2F_2) [*Zander et al.*, 1992; *Montzka et al.*, 1999; *Nassar et al.*, 2006] with more recent contributions from HCFC-22 ($CHClF_2$) [*O'Doherty et al.*, 2004; *Nassar et al.*, 2006], since CFC-11 and CFC-12 emissions from the ground have been progressively phased out by the Montreal Protocol and its subsequent amendments. The long tropospheric lifetimes of these fluorine source compounds allow them to be transported into the lower stratosphere, where the photolysis of CFC-11 and CFC-12 leads to the formation of the two temporary reservoirs chlorofluoroformaldehyde (COClF) and carbonyl fluoride (COF_2) which are characterized by lifetimes on the order of months in the lower stratosphere [*Chipperfield et al.*, 1997]. Studies dealing with measurements of COF_2 or COClF using ground-based, in situ or spaceborne techniques include those by *Wilson et al.* [1989], *Zander et al.* [1994], *Mélen et al.* [1998], *Nassar et al.*

---

[1] Institute of Astrophysics and Geophysics of the University of Liège, Liège, Belgium.
[2] Institute for Meteorology and Climate Research, Karlsruhe Institute of Technology, Karlsruhe, Germany.
[3] Institute for Climate and Atmospheric Science, School of Earth and Environment, University of Leeds, Leeds, UK.
[4] Department of Chemistry, University of York, York, UK.
[5] Department of Chemistry, University of Waterloo, Waterloo, Ontario, Canada.
[6] Department of Physics, University of Toronto, Toronto, Ontario, Canada.

[2006], *Fu et al.* [2009] and *Duchatelet et al.* [2009]. Subsequent photolysis of COF_2 and $COClF$ then releases F atoms, which can quickly react with CH_4, H_2O or H_2 to form the extremely stable hydrogen fluoride (HF) gas, thus preventing a catalytic ozone destruction cycle involving fluorine [*Stolarski and Rundel*, 1975]. The formation of HF by these reactions is significant, as they make HF the largest fluorine reservoir in the middle and upper stratosphere. For example, near 40 km at midlatitudes, HF contributes almost 80% to the total inorganic budget F_y [see *Nassar et al.*, 2006, Figure 4a]. The extreme stability of HF also makes this gas an excellent tracer of air mass transport and subsidence in the lower stratosphere [*Chipperfield et al.*, 1997]. The main sinks of stratospheric HF are its slow diffusion into the troposphere, with eventual rainout, and its upward transport into the mesosphere, where it is destroyed by photolysis.

[3] *Zander* [1975] was the first to detect the presence of HF in the Earth's atmosphere. Since then, several studies dealing with HF total column amounts derived from ground-based infrared solar observations at several latitudes in both hemispheres have been published [e.g., *Zander et al.*, 1987; *Reisinger et al.*, 1994; *Notholt et al.*, 1995, *Rinsland et al.*, 2002]. In addition, recent years have seen the emergence of more sophisticated retrieval algorithms allowing vertical distributions as well as partial column abundances to be determined from FTIR spectra recorded at ground-based stations affiliated with the Network for the Detection of Atmospheric Composition Change (NDACC; see http://www.ndacc.org). Illustration of such HF products is provided by, for example, *Barret et al.* [2005], *Mahieu et al.* [2008] and *Senten et al.* [2008]. Vertical distributions of hydrogen fluoride have also been measured by a large number of balloon, aircraft and space experiments [e.g., *Coffey et al.*, 1989; *Toon et al.*, 1992; *Zander et al.*, 1992; *Sen et al.*, 1996; *Considine et al.*, 1999; *Nassar et al.*, 2006]. In particular, HF data gathered during four missions of the Atmospheric Trace Molecule Spectroscopy (ATMOS) [*Gunson et al.*, 1996] and by the Halogen Occultation Experiment (HALOE) [*Russell et al.*, 1993] from 1991 to 2005 have provided a significant set of global HF vertical distribution measurements. Since then, the Atmospheric Chemistry Experiment Fourier Transform Spectrometer (ACE-FTS) [*Bernath et al.*, 2005] is the only space instrument currently monitoring most of major source and sink fluorine-containing gases (including HF) on a global scale. All of these ground-based or space observations have provided important information on the HF column amounts and vertical distributions, its seasonal and latitudinal dependence, its temporal trends and are of great interest for direct comparisons with numerical model calculations [see, e.g., *Rinsland et al.*, 1991; *Chipperfield et al.*, 1997; R. Ruhnke et al., Measured and simulated time evolution of HCl, ClONO2, and HF total columns, manuscript in preparation, 2010].

[4] Despite the fact that fluorine does not directly participate in ozone depletion, measurements of the concentrations of individual F-containing species in different altitude ranges of the atmosphere are important as they reflect the amounts of anthropogenic gases–which often also contain ozone-depleting chlorine and/or bromine atom(s)–transported into the middle atmosphere. In addition, as anthropogenic surface emissions of F-containing species are continually evolving [e.g., see *World Meteorological Organization* (*WMO*), 2007, Table 1-7], the study of long-term fluorine time series is mandatory as this helps in the assessment of the magnitude and development with time of their release to the atmosphere. The main purpose of this paper is to present a 26 year time series of HF total vertical abundances derived from FTIR ground-based solar observations performed at the high-altitude International Scientific Station of the Jungfraujoch (hereafter ISSJ; 46.5°N, 8.0°E, 3580 m above sea level (asl)), an Alpine station located in the Swiss Alps and affiliated with the NDACC since 1989.

[5] In section 2, we first give a complete overview of the retrieval strategy adopted for our FTIR spectra inversion. In particular, we compare HF total vertical abundances derived from two different retrieval algorithms (namely, SFIT-2 and PROFFIT). We further quantify the impact of the line shape model adopted to simulate HF absorption lines (Voigt or Galatry line shape models) on HF retrieved total columns and vertical profiles as well as on fitting quality. This section also provides a typical HF error budget. In section 3, we compare our FTIR HF partial columns (and total columns, as far as possible) to corresponding products derived from satellite observations (namely, HALOE and ACE-FTS; see section 3.1) and from two three-dimensional (3-D) chemical transport model (CTM) simulations (SLIMCAT and KASIMA; see section 3.2). In addition, FTIR and CTMs time series are further analyzed in order to derive the main characteristics of the HF seasonal cycle at different altitudes. Comparisons with previous studies are also included. Section 3 closes with a correlation study between HF seasonal variation and the tropopause height cycle above Jungfraujoch.

2. HF Observational Database and Retrieval Strategy

[6] All the results produced in this study have been derived from high-resolution solar spectra recorded at ISSJ under clear-sky conditions with two FTIR spectrometers between March 1984 and December 2009. From 1984 onward, observations were made with a homemade (HM) FTIR spectrometer, backed since 1990 by a commercial Bruker-120 HR instrument. The observational database analyzed here consists of a subset of all spectra recorded with solar zenith angles (SZA) up to 85° and that encompass the R(1) line (4038.965 cm^{-1}) of the fundamental 1–0 band of HF (see Table 1 for precise microwindow limits and interfering gases). The HF line used here is probably the best transition for ground-based monitoring purposes as its spectroscopic parameters are well known [*Pine et al.*, 1985], allowing HF column abundances to be accurately determined. This line is therefore commonly adopted for HF retrievals by FTIR ground-based stations [e.g., see *Mahieu et al.*, 2008, Table 3]. Moreover, retrieval tests have also demonstrated that the adoption of additional HF microwindows (e.g., that encompass HF lines near 4000 or 4109 cm^{-1}) often provides a benefit for the information content, balanced however by a significant deterioration of the global fit residuals. Additional statistics concerning our FTIR database are provided in Appendix A1.

Table 1. HF Microwindow Used for Our FTIR Retrievals

Range (cm^{-1})	Interfering Species[a]
4038.81–4039.07	H_2O, HDO, CH_4

[a]"Interfering Species" lists the interfering gases whose vertical distributions are adjusted during the retrieval process.

2.1. A Priori Information

[7] The adopted a priori HF profile is a zonal mean (for the 41°N–51°N latitude band) of almost 800 occultations recorded by the ACE-FTS instrument between February 2004 and July 2008 (see Figure 1, left). These occultations are the version 2.2 of ACE-FTS products and corresponding HF measurements extend from about 14 km to 55 km. Above 55 km, the same a priori HF information used by ACE-FTS during its retrieval procedure has been adopted. For the lowest altitude levels (i.e., between the altitude site and 14 km), we have kept, for each individual profile, a constant value equal to the HF VMR value recorded by the ACE-FTS instrument at 14 km. Based on this climatological data set, a full a priori covariance matrix S_a has been constructed. The (i,j) element of such covariance matrix is given, per definition, by

$$S_a(i,j) = E[(VMR_i - \overline{VMR_i}) \times (VMR_j - \overline{VMR_j})], \quad (1)$$

where VMR_k represents the kth element of a given VMR column vector, $\overline{VMR_k}$ stands for the kth element of the mean VMR column matrix and E denotes the mathematical expectation, i.e., $E = \frac{1}{N} \cdot \sum_{i=1}^{N} y_i$, if we consider a set including N measurements vector $y_{i.}$. Since the covariance matrix we have obtained by using equation (1) with ACE-FTS climatological profiles was singular (noninvertible), 20% uncorrelated noise has been added to its diagonal elements. Figure 1 (right) illustrates the corresponding HF a priori variability profile, which corresponds to the diagonal elements of the S_a matrix.

2.2. Fitting Algorithm

[8] Our HF inversions have been performed with the PROFFIT v.9.5 algorithm, a code specifically developed at IMK-ASF, Karlsruhe, Germany, to derive total or partial columns and vertical profiles of atmospheric gases from high-resolution FTIR spectra [*Hase et al.*, 2004]. With PROFFIT, the target gas as well as each interfering species can be fitted by applying, independently for each gas, one of the three following inversion techniques: (1) the optimal estimation method (OEM) [*Rodgers*, 2000]; (2) a Tikhonov-Phillips (TP) regularization [*Tikhonov*, 1963; *Phillips*, 1962]; or (3) a scaling approach. In addition, when one of
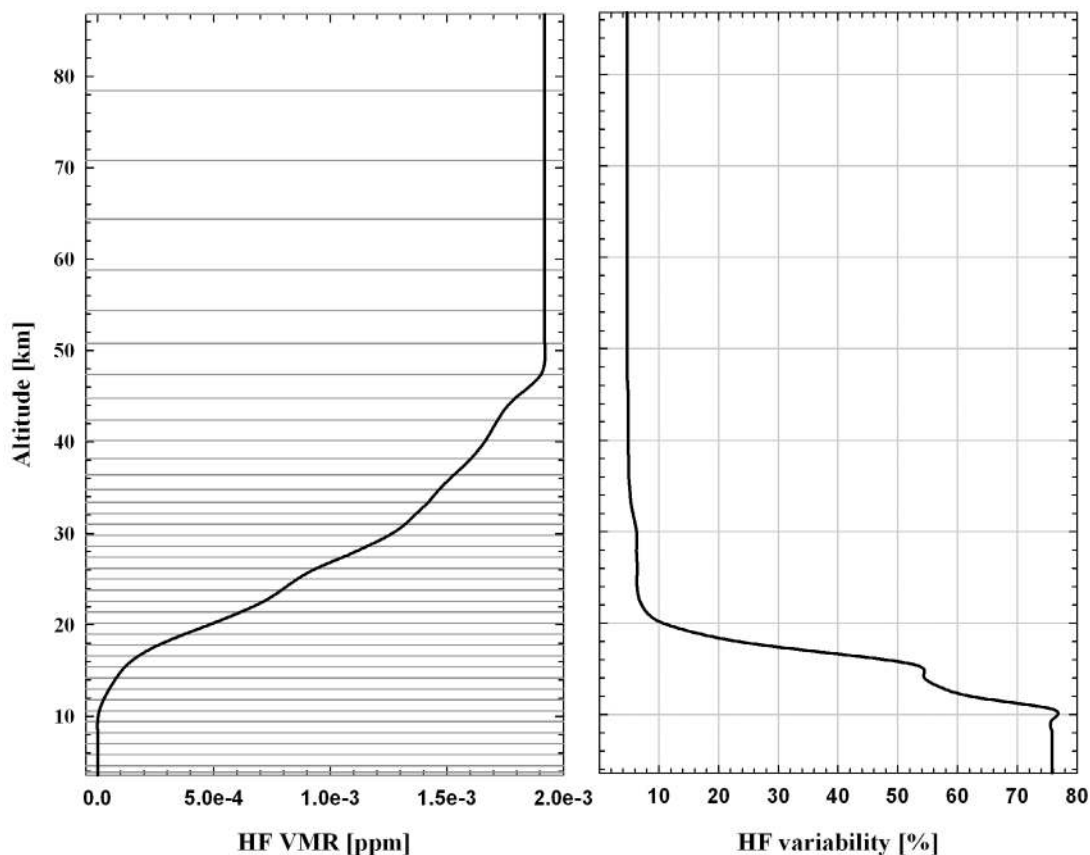

Figure 1. (left) A priori HF VMR profile and (right) corresponding variability profile (diagonal elements of S_a matrix) adopted for our FTIR HF retrievals. They are based on ACE-FTS measurements in the 41°N–51°N latitude band. Background solid lines of Figure 1 (left) reproduce the 41-layer scheme adopted for the retrieval procedure.

the two first regularization techniques is selected, the code can also perform inversions on a logarithmic vertical scale, in order to avoid nonphysical negative VMR values. The 9.5 version of PROFFIT also includes a module that allows a complete error budget to be established including contributions of the leading systematic or statistical (random) errors. A more detailed description of the PROFFIT code is provided by *Hase et al.* [2004].

[9] Since the SFIT-2 algorithm [*Rinsland et al.*, 1998] is the code most commonly used within the FTIR community to retrieve vertical abundances of atmospheric gases, we have found it useful to compare PROFFIT HF total column results with those generated by applying the SFIT-2 v3.91 algorithm. Such an intercomparison exercise has already been performed by *Hase et al.* [2004] for four atmospheric gases, including stratospheric (namely: ozone and HNO_3) and tropospheric (namely: HDO and N_2O) species, which are also characterized by different types of spectral signatures and by diverse spatial variability. Based on a typical set of three FTIR spectra recorded at two high-latitude NDACC affiliated sites (Thule, 76.5°N, 68.7°W, 225 m asl and Kiruna, 67.8°N, 20.4°E, 420 m asl), *Hase et al.* [2004] have demonstrated the very good agreement found for retrieved total columns and retrieved vertical profiles of the four target gases, despite the fact that SFIT-2 and PROFFIT differ, notably in terms of ray tracing and radiative transfer algorithms. In particular, when similar regularization constraints are applied, the difference between total columns retrieved from both codes is within 1% for all gases under investigation.

[10] For our own SFIT-PROFFIT intercomparison, we have adopted the following regularization parameters and ancillary inputs: (1) HF microwindow limits and interfering gases, as specified in Table 1: while an OEM procedure is applied for HF, VMR profiles of all interfering gases are simply scaled; (2) a priori knowledge of HF (mean profile and covariance matrix) as described in section 2.1: similar a priori VMRs have also been adopted for the three interfering gases; (3) the official HITRAN 2004 spectroscopic linelist [*Rothman et al.*, 2005]; (4) the pressure-temperature (p-T) profiles adopted during the retrievals are those provided by the National Centers for Environmental Prediction (NCEP, Washington, DC.; see http://www.ncep.noaa.gov), specifically computed for the ISSJ site on a daily basis; and (5) all FTIR spectra recorded at ISSJ during 2005 and including the R(1) line of HF. The year 2005 has been selected because of (1) the large number of observations (~200) available that year and (2) the fact that special atmospheric events, like, e.g., a polar vortex overpass, have occurred in 2005 above ISSJ.

[11] Under these retrieval conditions, we have found a nonsignificant mean relative difference in HF total columns (computed as [(SFIT-PROFFIT)/PROFFIT] × 100) equal to −0.99 ± 1.02%, which is in excellent agreement with values reported by *Hase et al.* [2004]. The largest discrepancy (in absolute value) reaches 4.82%. For the three observations recorded on 27 January (which corresponds to a vortex overpass above ISSJ [see *Duchatelet et al.*, 2009, Figure 4], the relative difference between both codes is close to 3%, with PROFFIT HF total columns being higher than those retrieved with SFIT-2. Concerning interfering gases, it is important to mention that negative VMR values (mainly

for HDO whose absorption in the HF microwindow at 4038 cm^{-1} is very weak at the high-altitude site of the Jungfraujoch) have been frequently derived with both codes. For example, for HF retrievals performed with SFIT-2, we have noticed negative HDO total columns in almost 20% of occurrences. For this reason we have decided to constrain all interfering gases with a TP first-order smoothing regularization including a logarithmic vertical scale in our final HF PROFFIT retrieval strategy. For HF, we have kept the OEM approach including a priori information illustrated in Figure 1 but we have also worked on a logarithmic scale, for consistency.

2.3. Choice of Line Shape Model

[12] In the version 3.91 of SFIT-2, the direct model assumes a Voigt profile for the absorption line shape of each atmospheric gas. This profile takes simultaneously into account the perturbing influences of neighboring particles (pressure broadening effect) as well as the thermal translational motion of the target gas itself (Doppler broadening effect). The first effect leads to Lorentzian line shapes while the second one generates Gaussian line shapes. A Voigt profile is consequently given by the convolution of a Lorentz function with a Gaussian one. However, as atmospheric molecules are also hindered in their free motion by collisions with the buffer gas, one can observe a narrowing of the Doppler component of the line shape. This collision-induced narrowing effect, most commonly known as the "Dicke effect" or "Dicke narrowing," has been described for the first time by *Dicke* [1953] and by *Wittke and Dicke* [1956]. For most atmospheric molecules, this effect is weak, except for species with a free mean path greater than the wavelength of their transitions. According to *Chou et al.* [1999], this happens for HF when the pressure is less than 290 hPa (i.e., for altitudes approximately greater than 10 km).

[13] Analytical models simultaneously including the Doppler broadening effect and the collision-induced narrowing effect exist and have been developed, for example, by *Galatry* [1961] ("soft" model) and by *Rautian and Sobel'man* [1967] ("hard" model). *Barret et al.* [2005] were the first to introduce such concepts in the direct model of an inversion algorithm of FTIR spectra (this code is called Atmosphit and has been developed at Université Libre de Bruxelles, Brussels, Belgium) to quantify the impact of the line narrowing effect on the retrievals of HCl and HF. It has been demonstrated by *Barret et al.* [2005] that, for HF inversions from its R(1) line performed with FTIR spectra recorded at Jungfraujoch, the introduction of the collisions-induced narrowing effect leads to smoother retrieved vertical profiles, mainly between 30 and 35 km. As a direct result, *Barret et al.* [2005] found that the agreement of such FTIR HF profiles with HALOE HF distributions improved and was more consistent with altitude, with a mean relative difference which does not exceed 10% between 15 and 50 km [see *Barret et al.*, 2005, Figure 7]. In addition, *Barret et al.* [2005] also mention that this spectroscopic effect is almost without any consequence for HF retrieved total columns, with differences (relative to HF total columns obtained with a Voigt model) lower than 1%. In terms of spectral simulation quality, the differences they have obtained between synthetic spectra generated with the two line shape models are significant, especially in the
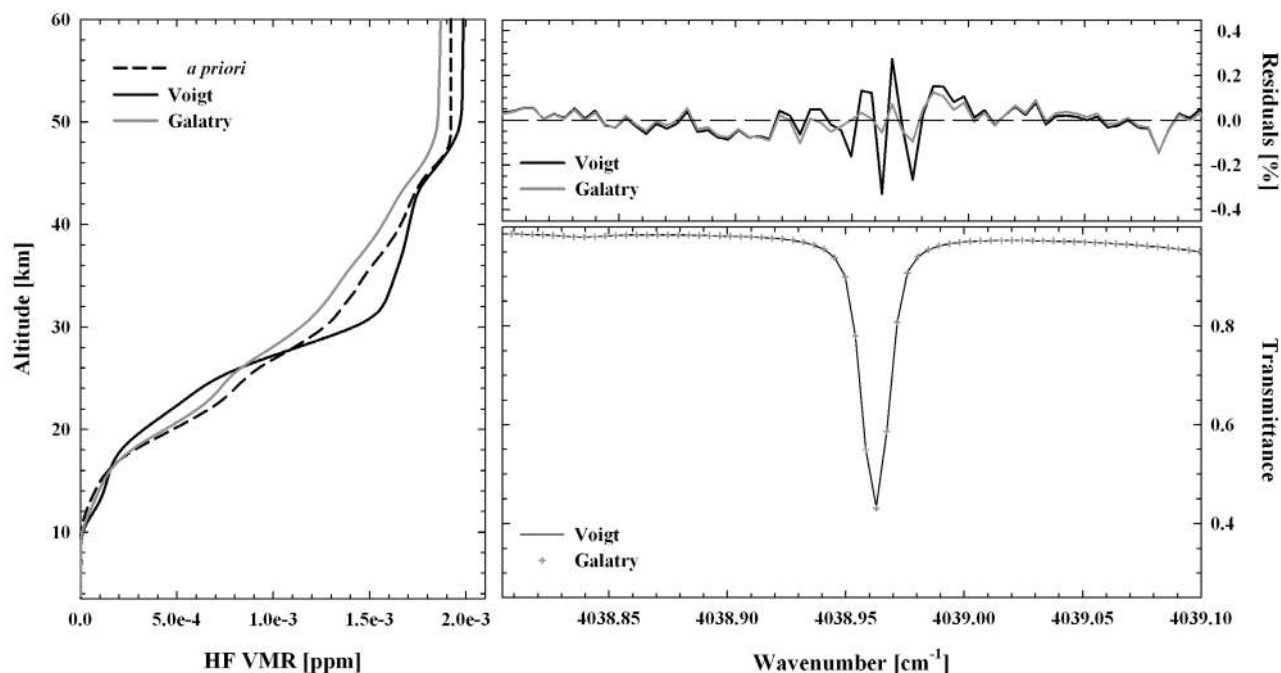
Figure 2. (left) Mean HF profiles (for the year 2005) retrieved with PROFFIT 9.5 and assuming Voigt line shape (black solid line) or Galatry line shape (gray line). The a priori profile adopted for the retrievals is reproduced with the dashed line. (bottom right) typical example of synthetic spectra obtained for HF with a Voigt model (black line) and with a Galatry model (gray crosses). These two spectra were calculated during the fit with PROFFIT 9.5 of a FTIR observation (not shown here) recorded at ISSJ on 8 January 2005 at a solar zenith angle close to 73° (spectral resolution = 0.0044 cm^{-1}). (top right) For each case, corresponding residuals (measured minus simulated spectrum) are plotted.

center of the HF line. *Barret et al.* [2005] report a relative difference between both models close to 3%, i.e., significantly larger than the spectral noise value [see also *Barret et al.*, 2005, Figure 4 (right)].

[14] In addition to the Voigt model, the version 9.5 of PROFFIT is also able to perform retrievals including a Galatry "soft collision" model. Even if these two line shape models are not "speed-dependent" models, which is not strictly valid, this is a minor issue for HF, as demonstrated by *Pine and Ciurylo* [2001]. Concerning our own HF retrievals, comparisons between both line shape models (Voigt and Galatry) have been performed with the same set of FTIR spectra used for the intercomparison of SFIT-2 with PROFFIT (see section 2.2). As in *Barret et al.* [2005], we have observed a significant smoothing of HF profiles when the Galatry model is used, mainly between 25 and 40 km (Figure 2, left). A small but significant relative difference (computed over the whole year 2005) between corresponding HF total columns of $1.18 \pm 0.29\%$ was found (the error corresponds to $1\,\sigma$ standard deviation), in good agreement with *Barret et al.* [2005]. Regarding fitting quality, a typical example of fit residuals is given in the top frame of Figure 2 (right). A significant improvement is obtained when the Galatry model is adopted. In particular, systematic symmetric features observed in the center of the HF signature when the Voigt model is used are significantly reduced with the Galatry approach. The mean relative difference (for all FTIR observations of 2005) calculated as [(Voigt-Galatry)/Galatry] × 100 between fitting residuals obtained with both models is $18.97 \pm 13.17\%$ ($\pm 1\,\sigma$ standard deviation). This result highlights the fact that a Galatry line shape model definitely improves HF retrievals quality: it was consequently adopted in our final HF retrieval strategy with PROFFIT, whose main input parameters are summarized in Appendix A2.

2.4. Information Content and Error Budget

[15] Based on the information content analysis provided in Appendix A3, we have demonstrated that the DOFS characterizing our Bruker FTIR HF retrievals is around 3.0, which justifies the definition of three independent HF partial columns. As illustrated by AvK of Figure A1 (Appendix A3), these three partial columns cover different regions of the stratosphere. The first one approximately extends from 10 to 17 km and covers the lowermost part of the stratosphere. Hereafter, we will refer to this partial column by using the acronym LMS (lowermost stratosphere). The second partial column roughly extends from 17 to 25 km and will be further denoted by MS (lower-middle stratosphere). Finally, the third partial column covers the middle-upper part of the stratosphere (approximately from 25 to 40 km) and will be reported as US (middle-upper stratosphere).

[16] We have further deduced with PROFFIT 9.5 a typical HF error budget from 5 FTIR Bruker spectra whose main characteristics are summarized in Table A4 in Appendix A4. These spectra have been selected in order to cover a wide range of SZA and to include FTIR observations performed at different times of the year and recorded at various periods in our time series. The error module of PROFFIT 9.5

Table 2. Error Sources Taken Into Account in Our HF Error Budget With PROFFIT 9.5

Error Type	Error Quantity[a] (%)	SYS[b]	STA[b]
Spectroscopy[c]	5.0, 2.0	1.0	0.0
Temperature profile[d]	1.0, 2.0, 5.0	0.3	0.7
Solar parameters[e]	1.0, 10^{-4}	0.2	0.8
LOS	1.0	0.1	0.9
ILS[f]	5.0	0.5	0.5
Baseline[g]	0.1, 0.0	0.5	0.5
Spectral noise	–	0.0	1.0

[a]Error quantity provides a priori error values assumed during the error estimation.

[b]SYS and STA give systematic and statistical weights, respectively, adopted for each error type.

[c]First value is for line intensity. Second value is for line half width.

[d]Error quantities are given in kelvin. First value is for altitudes below 10 km. Second value is for altitudes between 10 and 40 km. Third value is for altitudes above 40 km.

[e]First value is for line intensity. Second value is for spectral abscissa scale.

[f]Same values have been adopted for modulation and phase errors.

[g]First value is for offset error. Second value is for channeling error.

estimates individual contributions associated with seven different error sources: the spectroscopy (including both half-width and line intensity errors), the temperature profile, solar parameters (including line intensity and spectral shift), the line of sight (LOS), the instrumental line shape (ILS, including both modulation and phase contributions), the baseline (including both offset and channeling contributions) and the spectral noise. For each error type (except for the spectral noise error, which is directly estimated from FTIR spectra during the retrieval process), Table 2 provides our estimates of input uncertainties (in percent, except for those labeled) which consist of reasonable error values assumed during the error estimation. Error quantities associated with spectroscopic uncertainties are in line with error indices referenced in the original HITRAN 2004 file for the R(1) HF line [*Rothman et al.*, 2005]. For ILS error, error values are based on HBr cell spectra retrievals performed with the LINEFIT v.8.2 code [*Hase et al.*, 1999]. In addition, since no channeling features were found in the HF region of our FTIR spectra, the corresponding error quantity has been set to zero. The two last columns of Table 2 also provide the weighting factors adopted in our error analysis in order to define systematic (SYS) and statistical (STA) contributions of each error type. Colored solid lines of Figure 3 reproduce the individual contributions to the error budget (in ppm) characterizing our HF retrievals below 60 km, for each error source reported in the legend (left panel is for systematic errors, right panel is for statistical errors). These error distributions correspond to mean profiles averaged over the 5 FTIR observations reported in Table A4 (see Appendix A4) and have been obtained under the assumptions summarized in Table 2. To appreciate more easily the contribution of each error type, the HF a priori profile has also been plotted in Figure 3 (left and right). While the error associated with HF spectroscopic parameters is the main source of systematic error in almost the entire altitude range, the spectral noise error dominates statistical errors below 25 km. Above 25 km, statistical errors due to spectral noise, ILS, LOS and temperature profile are about the same order of magnitude. For both systematic and statistical errors, the contribution of baseline and solar parameter

errors remains smaller than other error sources, reflecting the very good definition of the zero absorption level of our FTIR spectra and the weak interferences by solar lines in our HF microwindow, respectively. All details regarding the error budget characterizing our HF total and partial columns are provided in Appendix A4.

3. FTIR HF Time Series at Jungfraujoch and Intercomparison

[17] As the information content associated with our Bruker observations is greater than the one characterizing our homemade spectra (see Appendix A3), we have selected the Bruker time series for studies dealing with partial columns and we have consequently adopted partial column limits obtained from the Bruker information content analysis (i.e., LMS, MS and US vertical abundances). The density measurements associated with our Bruker time series is also significantly greater (in particular, after 1996) and therefore more appropriate to such a comparison exercise. Homemade observations have however been kept when HF total columns are compared. It is thus crucial to first check the consistency between our two FTIR databases. For the 94 coincident measurement days available between January 1996 and January 2008, we have compared daily mean HF total columns derived from our two spectrometers and have found a mean relative difference ($\pm 1\ \sigma$ standard deviation) computed as [(Bruker-HM)/HM] × 100 equals to 0.93 ± 2.21%. Considering this very good agreement, time series derived from both instruments have been merged in further comparisons including HF total vertical abundances. For information, comparisons on partial columns have also been performed, with altitude ranges for partial columns computation being those derived from the HM information content analysis. Mean relative differences ($\pm 1\ \sigma$ standard deviation) characterizing HF 10–20 km and 20–40 km partial columns are equal to -11.49 ± 14.86 and 8.26 ± 9.71, respectively, and are consequently also not significant. Finally, additional tests have also been performed in order to check the consistency between HF quantities derived from HM spectra recorded with different optical filters. Coincident measurement days exist only for the two last HM filters described in Table A1 in Appendix A1. For these 166 coincident days, relative differences in HF daily mean total and partial columns do not exceed 0.6%.

3.1. FTIR Versus Space Data

[18] We have compared our PROFFIT daily means HF partial columns to coincident daily mean occultations performed in the 41°N–51°N latitude band by the two satellite instruments HALOE and ACE-FTS. The HF HALOE data are the v19 products and cover the 1991–2004 time period while the version 2.2 of ACE-FTS data between 2004 and 2009 has been used. For each instrument, both sunset and sunrise occultations have been retained. The good consistency between sunset and sunrise HF measurements has been previously demonstrated by *Russell et al.* [1996] for HALOE and by *Mahieu et al.* [2008] for ACE-FTS. Once daily mean profiles have been computed, the HALOE (ACE-FTS) data set includes almost 800 (160) mean profiles for which almost 100 (40) coincident FTIR measurements are available. It is worth mentioning that only MS and
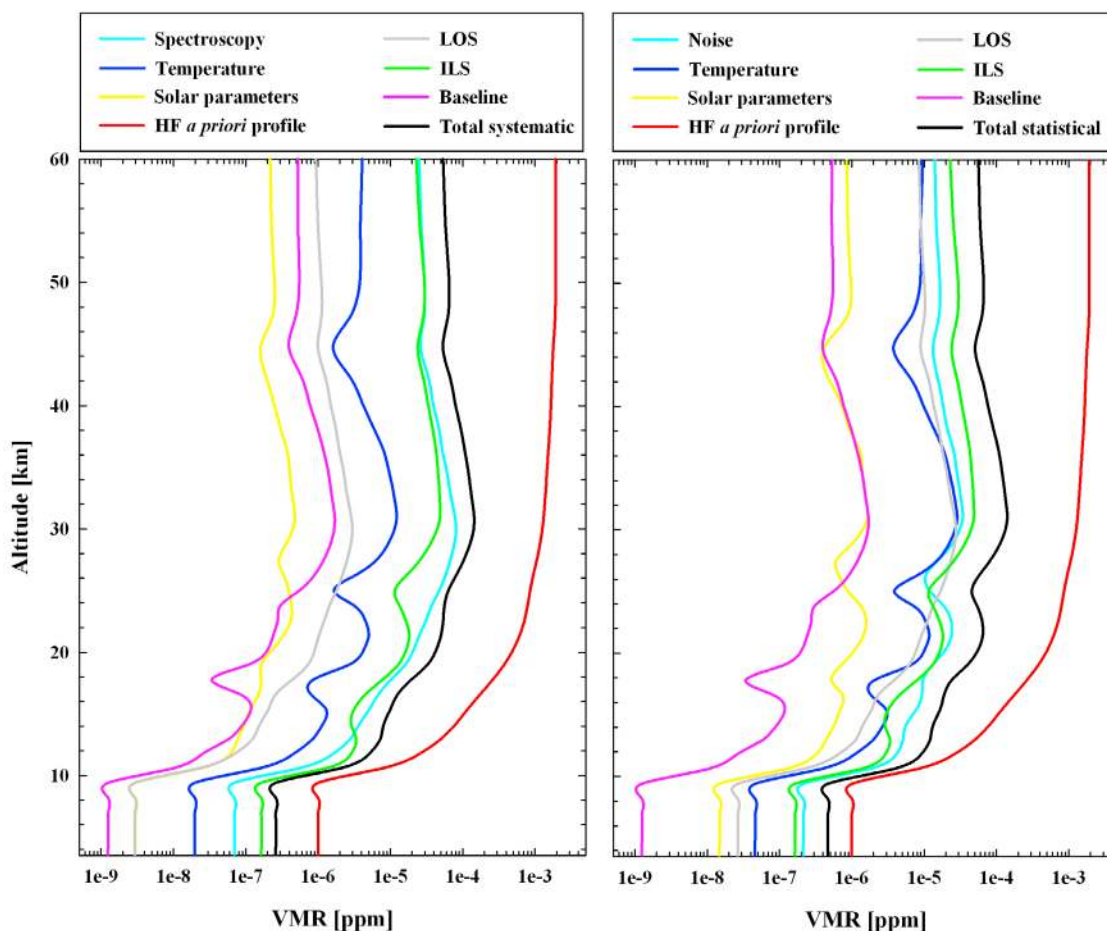
Figure 3. HF error budget obtained with PROFFIT 9.5 below 60 km, for the different (left) systematic and (right) statistical error types reported in Table 2. To ease the evaluation of the contribution of each error source to the budget, the HF a priori profile has also been plotted in red. The error budget plotted here has been obtained by averaging individual error profiles derived from each FTIR spectra reported in Table A4 (Appendix A4).

US abundances have been compared here, as HF vertical profiles recorded by HALOE (ACE-FTS) typically cover the 15–60 km (14–55 km) altitude range and hence do not allow LMS or total column comparisons. As HALOE profiles are defined on a vertical pressure grid, corresponding MS and US partial columns have been calculated for pressure levels ranging from 85 to 25 hPa and from 25 to 2.5 hPa, respectively. Regarding ACE-FTS VMR profiles, they have been first interpolated on the same layering as used for our FTIR retrievals before being converted into partial columns. For both HALOE and ACE-FTS, the conversion from each individual VMR profile to partial column abundances has been performed by using corresponding pressure and temperature profiles simultaneously measured by these two instruments [*Russell et al.*, 1993; *Boone et al.*, 2005].

[19] Figure 4 displays time series of daily mean HF MS (Figure 4, bottom) and US (Figure 4, top) vertical abundances deduced from our Bruker FTIR measurements (gray dots) as well as coincident daily means computed from HALOE (white triangles) and ACE-FTS (white diamonds) space occultations. As our FTIR a priori information is based on climatological data by ACE-FTS (see section 2.1),

we have judged it necessary to also reproduce FTIR a priori partial columns (gray crossed dots) for the comparison between our FTIR partial columns and those deduced from ACE-FTS. For both MS and US abundances, statistical results for comparisons between ground-based and space data sets are summarized in Table 3. Mean relative difference values (Δ) reported in Table 3 have been computed as [(FTIR-satellite)/satellite] × 100. These relative differences are also characterized by their standard deviations around the mean (σ). Table 3 shows that no significant bias exists between FTIR and HALOE observations, for both altitude ranges under consideration here. The larger values found from the ground-based data are also consistent with the ATMOS-HALOE comparison made by *Russell et al.* [1996] during the validation phase of this latter space instrument. Indeed, these authors mention that above 15 hPa (which corresponds to an altitude of around 30 km), HALOE HF VMR profiles are about 10% lower than those measured by ATMOS. Below the 15 hPa level, the ATMOS-HALOE mean difference increases to reach a maximum value close to 35% in the lower stratosphere. The same conclusion can be drawn when *Russell et al.* [1996] compared HF HALOE VMRs with correlative HF vertical profiles recorded during
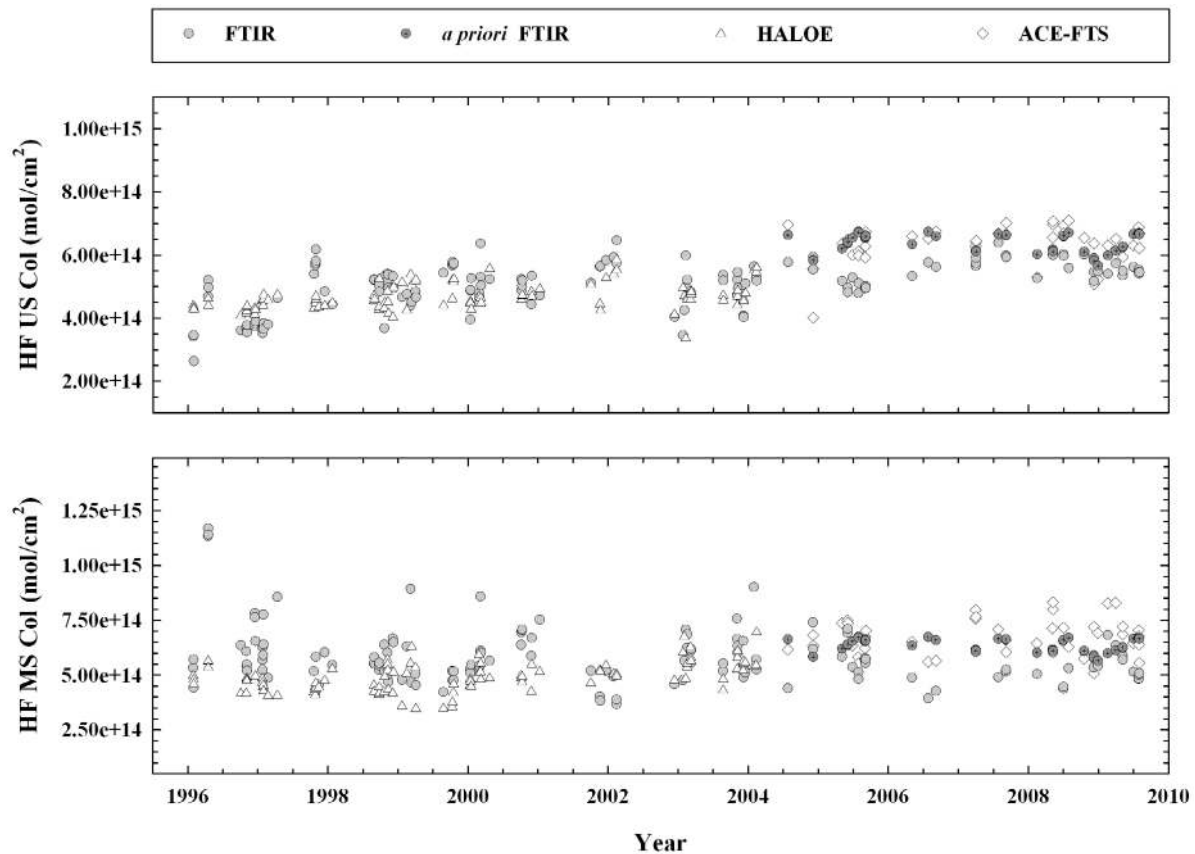
Figure 4. (bottom) Low-middle stratospheric and (top) middle-upper stratospheric HF partial columns as observed at Jungfraujoch by FTIR technique (gray dots) and by space occultations (HALOE: white triangles; ACE-FTS: white diamonds). All data points correspond to daily mean values for coincident measurement days between ground-based and space observations. Grey crossed dots reproduce initial guess values adopted during FTIR retrievals with the PROFFIT code.

balloon flights: the mean difference is lower than 7% from 5 hPa (~35 km) to 50 hPa (~20 km) and increases with increasing pressure. Nevertheless, as already mentioned in section 2.3, *Barret et al.* [2005] indicate that FTIR HF profiles above Jungfraujoch and correlative HF HALOE profiles (that have been smoothed with FTIR AvK) agree within 10% between 15 and 50 km, as a direct consequence of the introduction of a Galatry line shape model in the FTIR retrieval strategy. Even if a Galatry model was adopted in our own retrieval procedure, we presently do not observe such good agreement between FTIR and HALOE partial amounts below 25 km. To try to explain this remaining difference, we have first restricted our spatial criterion adopted to select HALOE occultations, according to *Barret et al.* [2005]: only HALOE profiles measured in the 43.5°N–49.5°N × 3°E–13°E rectangle were retained. This new criterion assures that all HALOE occultations selected are located within 340 km (560 km) in latitude (longitude) around the Jungfraujoch, i.e., within 655 km of the Jungfraujoch. Despite the fact that this criterion significantly reduces the number of coincident FTIR-HALOE measurements to 29 (the number of coincidences in the work by *Barret et al.* [2005] reaches 21), it is in agreement with the last line of Table 4 of *Mahieu et al.* [2008] that indicates that a spatial criterion within 1000 km is still too

large for that kind of comparison. Under these conditions, the mean FTIR-HALOE relative difference values reported in Table 3 becomes 18.4 ± 18.2% and −2.3 ± 12.7% for MS and US regions, respectively. Finally, once these 29 HALOE profiles are smoothed with a typical FTIR averaging kernel matrix (the one for which partial column kernels are illustrated on Figure A1 in Appendix A3), HF MS and US partial abundances are in very good agreement, with mean relative difference equal to 0.8 ± 19.4% and −4.0 ± 11.9%, respectively. This agreement is twice as good as the one deduced by *Barret et al.* [2005] and highlights the fact that a smoothing operation is desirable for a proper comparison between data derived from two instruments characterized by different vertical resolutions.

[20] In addition, comparisons made by *Russell et al.* [1996] with FTIR ground-based HF total columns above Jungfraujoch indicates that HALOE is able to clearly capture the HF annual cycle as well. That is also highlighted in Figure 4 (top and bottom), despite the fact that the HALOE instrument does not seem able to detect large excursions that occur at times in the MS range, predominantly during one or two days from December to April (see for example 1996, 1997, 1999, 2000 and 2004). As indicated by potential vorticity maps over Europe (provided by the European Center for Medium-Range Weather Forecasts (ECMWF);

Table 3. Statistical Means (Δ) and Standard Deviations (σ) of the Relative Difference Between the HF MS and US Daily Mean Partial Columns Derived From Our FTIR Measurements With the PROFFIT Code and Coincident Satellite Observations

Satellite	Δ (%)	σ (%)	N[a]
	MS (17–25 km)		
HALOE v19	21.7	28.9	101
ACE-FTS v2.2	−17.5	11.2	42
	US (25–40 km)		
HALOE v19	4.0	17.4	101
ACE-FTS v2.2	−12.0	11.8	42

[a]N denotes the number of comparisons involved in the statistics.

visit http://www.ecmwf.int/) at a potential temperature level of 475 K (which corresponds to an altitude close to 20 km), these large excursions are linked to HF-enriched air masses having moved above ISSJ from high northern latitudes.

[21] It also appears from Figure 4 and statistics of Table 3 that, for both altitude regions, a small but significant bias exists between FTIR and ACE-FTS data, with satellite partial columns being higher than those deduced from ground-based observations. *Mahieu et al.* [2008] were the first to compare ground-based FTIR HF data recorded at various sites (including ISSJ) with ACE-FTS products. In this ACE-FTS v2.2 measurements validation paper, these authors notably compare HF 12–27 km partial columns above Jungfraujoch with all coincident ACE-FTS occultations recorded between March 2004 and August 2007. Time and space criteria adopted for coincidence are ±24 h and 1000 km, respectively. To take into account the difference in vertical resolutions between both instrumentations, ACE-FTS partial columns have also been smoothed with typical FTIR averaging kernels. For the 20 coincident measurements available in their study, *Mahieu et al.* [2008] found a bias close to 7% between FTIR and ACE-FTS data. Even if the bias observed by *Mahieu et al.* [2008] is not significant, the same tendency as in the present study is however observed, i.e., the fact that HF ACE-FTS products seem to be higher than those deduced from FTIR ground-based observations at Jungfraujoch.

[22] In order to better compare our results with those published by *Mahieu et al.* [2008], we have also tightened our spatial criterion to ±3° latitude and ±5° longitude (i.e., the same criteria adopted in the second part of our FTIR-HALOE comparison). However, as this criterion reduces the number of coincidences between FTIR and ACE-FTS measurements to 5, we have kept the original 41°N–51°N latitude band and have relaxed the longitude criterion to ±8°. The corresponding 16 coincidences, all approximately located within 1000 km of the Jungfraujoch, lead to mean relative differences of −18.4 ± 7.9% and −14.0 ± 6.7%, for US and MS amounts, respectively; a smoothing operation applied to all coincident ACE-FTS profiles with a typical averaging kernel (the same adopted for the smoothing of HALOE profiles) transforms these two relative differences into −15.4 ± 6.1% and −15.8 ± 5.1%, respectively. Similar significant biases are thus observed in both stratospheric regions (with ACE-FTS giving higher HF abundances), the tightened spatial criterion and smoothing operation reduces significantly the standard deviation of these mean values.

The remaining difference with *Mahieu et al.* [2008] could perhaps be attributed to the difference in partial column limits used in the comparisons and to the absence of time criterion adopted in the present study. In addition, first comparison exercises involving ACE-FTS v3.0 products indicate a decrease of close to 5% in HF amounts (K. Walker, personal communication, 2010), that will probably reduce the two present biases to values close to −10%.

3.2. FTIR Versus Model Data

[23] Our daily mean FTIR HF partial columns have also been compared with daily values specifically computed for the Jungfraujoch location using two different state-of-the-art 3-D numerical models, namely the KASIMA (Karlsruhe Simulation model of the Middle Atmosphere) and SLIM-CAT CTMs. This time, the three HF partial columns (LMS, MS and US) are included in the comparison, as well as total vertical abundances.

[24] The KASIMA model used in this study is a global circulation model including stratospheric chemistry for the simulation of the behavior of physical and chemical processes in the middle atmosphere [*Reddmann et al.*, 2001; *Ruhnke et al.*, 1999]. The meteorological component is based on a spectral architecture with the pressure altitude $z = -H \ln\left(\dfrac{p}{p_0}\right)$ as vertical coordinate where H = 7 km is a constant atmospheric scale height, p is the pressure, and p_0 = 1013.25 hPa is a constant reference pressure. A horizontal resolution of T21 (about 5.6° × 5.6°) has been used. In the vertical regime, 63 levels between 10 and 120 km pressure altitude with a 0.75 km spacing from 10 up to 22 km and an exponential increase above were used. The meteorology module of the KASIMA model consists of three versions: the diagnostic model, the prognostic model and the nudged model which combines the prognostic and diagnostic model [*Kouker et al.*, 1999]. In the version used here, the model is nudged toward the operational ECMWF analyses of temperature, vorticity and divergence between 18 and 48 km pressure altitude. Below 18 km, the meteorology is based on ECMWF analyses without nudging, above 48 km pressure altitude, the prognostic model is used. The rate constants of the gas phase and heterogeneous reactions are taken from *Sander et al.* [2003]. The photolysis rates are calculated online with the fast-j2 scheme of *Bian and Prather* [2002]. The distributions of the chemical species in this model run were initialized on 30 April 1972, with data from a long-term KASIMA run.

[25] This study also uses results from the SLIMCAT 3D off-line CTM [*Chipperfield*, 2006]. The model is forced using winds and temperatures from meteorological analyses (e.g., ECMWF). The model uses a σ-θ vertical coordinate and in the stratosphere (θ level domain) vertical motion is diagnosed from calculated heating rates which gives a good representation of the slow stratospheric circulation [see *Monge-Sanz et al.*, 2007]. The model does not contain an explicit scheme for tropospheric convection and boundary layer mixing. Instead, the model assumes complete vertical mixing of species in the troposphere. The version used here is an updated version of the one used by *Feng et al.* [2007] to study long-term changes in ozone. The model was run at a resolution of 5.6° × 5.6° and 32 levels from the surface to ~60 km. The run extended from 1977 to 2010. From 1989
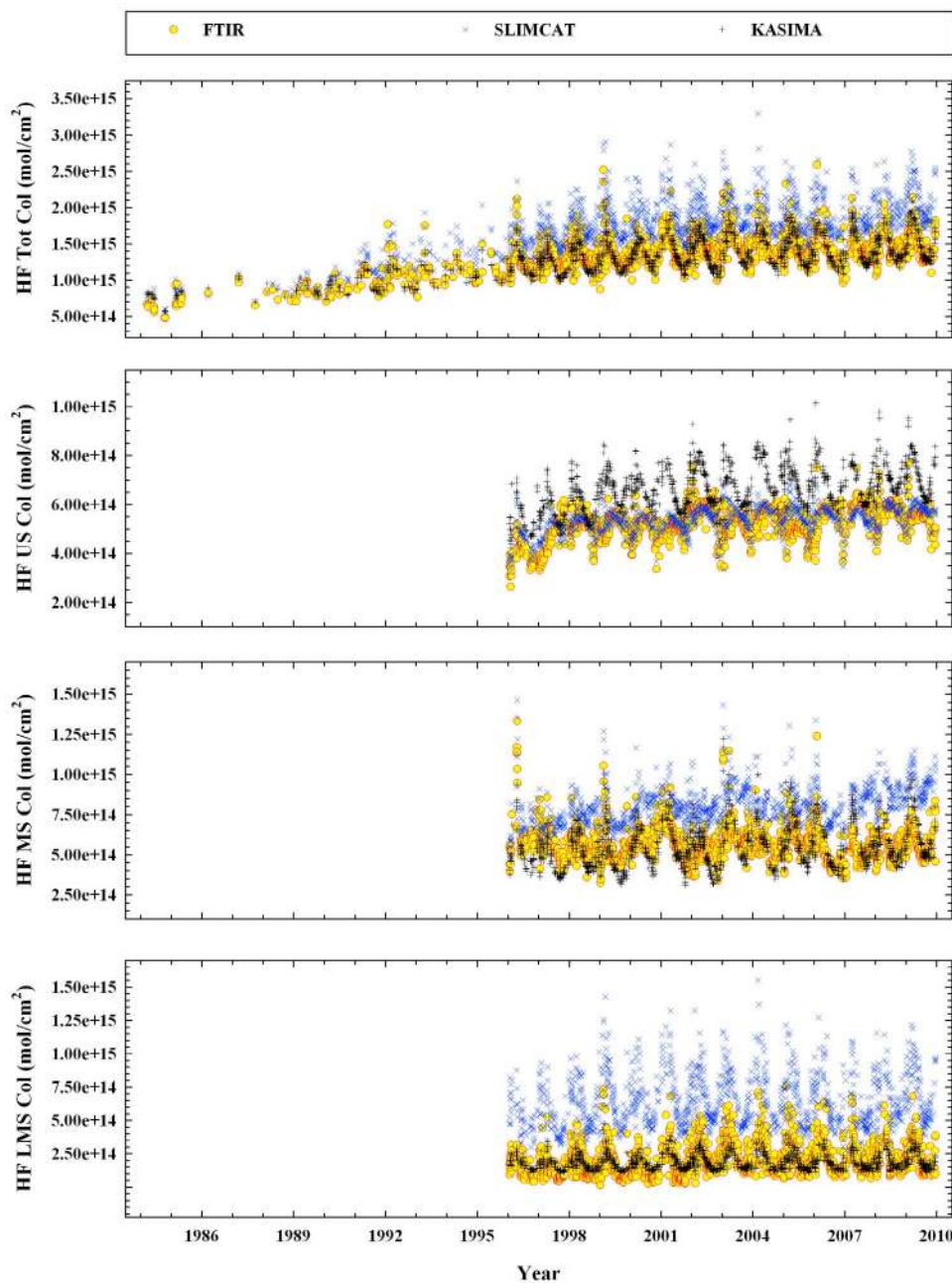
Figure 5. From bottom to top: lowermost stratospheric, lower-middle stratospheric, middle-upper stratospheric and total HF abundance time series derived from FTIR measurements with the PROFFIT code (yellow dots) and from SLIMCAT (blue crosses) and KASIMA (black crosses) CTMs. FTIR data points correspond to daily means values for all coincident days with daily CTM data.

onward, the period relevant for this study, the model was forced by ECMWF ERA-Interim reanalyses. The use of a continuous set of reanalysis data reduces the risk of spurious variations in the model tracer fields due to changes in meteorological input.

[26] The model has a detailed description of stratospheric chemistry. During the last years, SLIMCAT has already been exploited to perform comparisons of fluorine species abundances with satellite and ground-based observations [*Chipperfield et al.*, 1997]. More recently, it has also been used to derive long-term trends of atmospheric compounds

[*Feng et al.*, 2007] or for comparison with COF_2 measurements from ground-based FTIR [*Duchatelet et al.*, 2009]. The run included 10 halogenated source gases including the following fluorinated species CFC-11, CFC-12, $C_2Cl_2F_3$ (CFC-113), HCFC-22. The surface mixing ratio of these compounds was specified following *WMO* [2007]. For inorganic fluorine (F_y) the model treats COClF, COF_2 and, the ultimate degradation product, HF. The sink of HF is transport to the troposphere and an imposed near-zero surface mixing ratio.

Table 4. Statistical Means (Δ) and Standard Deviations (σ) of the Relative Difference Between the HF LMS, MS, US, and Total Daily Mean Abundances Derived From Our FTIR Measurements With the PROFFIT Code and Coincident Model Calculations

Model	Δ (%)	σ (%)	N[a]
LMS (10–17 km)			
SLIMCAT	−69.08	11.18	1335
KASIMA	3.41	38.48	1335
MS (17–25 km)			
SLIMCAT	−29.92	10.34	1335
KASIMA	7.01	18.94	1335
U.S. (25–40 km)			
SLIMCAT	−1.78	8.93	1335
KASIMA	−19.64	11.35	1335
Total (3.58–86.8 km)			
SLIMCAT	−22.54	6.55	1542
KASIMA	3.02	9.58	1542

[a]N denotes the number of comparisons involved in the statistics.

[27] Figure 5 displays FTIR and CTMs HF daily mean data for all coincident days available between years 1984 and 2009. However, for partial column comparisons, the time period is limited to the Bruker measurements (1996–2009), for reasons discussed in section 3.1. For total column comparisons, Bruker and HM FTIR data have been averaged in order to cover the full 1984–2009 time period. Table 4 provides mean relative difference values (Δ) computed as [(FTIR−model)/model] × 100 for LMS, MS, US and total HF vertical abundances. Those relative differences are here again characterized by their standard deviations around the mean (σ). The last column of Table 4 provides the number of data points involved in each comparison. It is clear from Figure 5 and Table 4 that the agreement between FTIR and KASIMA time series is excellent below 25 km as well as for HF total columns. A significant bias close to 20% exists for the middle-upper stratosphere region, with KASIMA giving higher column values than FTIR measurements. Regarding the FTIR-SLIMCAT comparisons, the contrary is observed, as the agreement is excellent for the 25–40 km partial columns and large significant biases exist for all other regions (including HF total columns which depend largely on the lower stratosphere). As the SLIMCAT model extends from the surface, the lower stratosphere is less constrained than the KASIMA model. Therefore problems in transport and chemistry in this region are more likely to manifest themselves.

[28] Each data set appearing in Figure 5 has also been analyzed in order to derive seasonal cycles associated to HF LMS, MS, US and total columns time series. This analysis has been performed with a statistical tool developed at the National Physical Laboratory (Teddington, UK) and based on a bootstrap resampling method that allows both the long-term and intra-annual variability of a given data set to be determined, including uncertainties affecting the trend value [*Gardiner et al.*, 2008]. This tool was notably used for the 1995–2004 trend analysis of CH_4, C_2H_6, CO, HCFC-22, N_2O and O_3 time series derived from six affiliated NDACC stations [*Gardiner et al.*, 2008], as part of the European project "Time Series of Upper Free Troposphere Observations from a European Ground-based FTIR Network" (UFTIR; see www.nilu.no/uftir) [*De Mazière et al.*, 2005]. It

is worth mentioning that the HF trend analysis is not included in the present study but will be addressed in a separate publication dealing with the inorganic fluorine budget above ISSJ and its long-term evolution (P. Duchatelet et al., Long-term evolution of inorganic fluorine budget above Jungfraujoch derived from FTIR measurements, manuscript in preparation, 2010). As given in equation (3) of *Gardiner et al.* [2008], the seasonal variability and the trend in an experimental time series are modeled by a function including both a linear component and a Fourier series. In the present study, a third-order Fourier series was used. Seasonal cycles deduced from total or partial HF time series of Figure 5 are illustrated in Figure 6. For each panel of Figure 6, gray dash-dotted curves are derived from our FTIR ground-based observations while black dashed curves and black dash-dotted curves reproduce seasonal cycles associated to SLIMCAT and KASIMA time series, respectively. Different panels of Figure 6 indicate that, except for the LMS region, the intra-annual variability deduced from the KASIMA model is the largest.

[29] In order to better compare the dashed curves of Figure 6, corresponding statistics are summarized in Table 5. For each altitude region and for each data set involved in our comparison, the date for which HF maximum and minimum vertical abundances are observed are given in the two first columns. The "Amplitude ($\times 10^{14}$ mol/cm^2)" column of Table 5 provides peak-to-peak amplitudes of each seasonal cycle, expressed in vertical column abundance units. These amplitudes have also been converted to percent values ("Amplitude (%)" column of Table 5) by applying the following approach: for each data set and each altitude range, HF yearly mean columns have been computed. For each year available for a given data set, the peak-to-peak amplitude (in column units) has then been simply expressed as a percentage of the corresponding HF yearly mean column. Values so deduced for each year have been finally averaged and appear in the last column of Table 5 (±1 σ standard deviation). Values between brackets correspond to two times the standard error on the mean.

[30] Except for the US region, a very close agreement between the maximum of the seasonal cycles of all data sets is found, with higher HF columns always observed during spring time. Concerning the HF minimum, the best agreement is found for total column values. For other altitude ranges, results are more spread. In any case, all data sets capture lower HF columns during the second half of the year. These results are in reasonably good agreement with those published by *Zander et al.* [1987] and based on 3 years (years 1983 to 1985) of FTIR HF total columns above Jungfraujoch. These authors have also noticed a strong seasonal cycle with peak values in February–March and a minimum that occurs between September and November.

[31] Regarding the amplitude of the seasonal cycle, no analysis is performed by *Zander et al.* [1987] but Figure 3 of this paper suggests a value that lies between 20 and 30%, in good agreement with the amplitudes reported in Table 5 for FTIR and SLIMCAT HF total columns. The value deduced from KASIMA runs is significantly higher. The same conclusion can be drawn when considering MS and US regions, with KASIMA amplitudes 2 to 4 times higher than those provided by SLIMCAT runs and FTIR measurements. Finally, both SLIMCAT and FTIR values indicate the same behavior in the stratosphere, i.e., that the amplitude of the
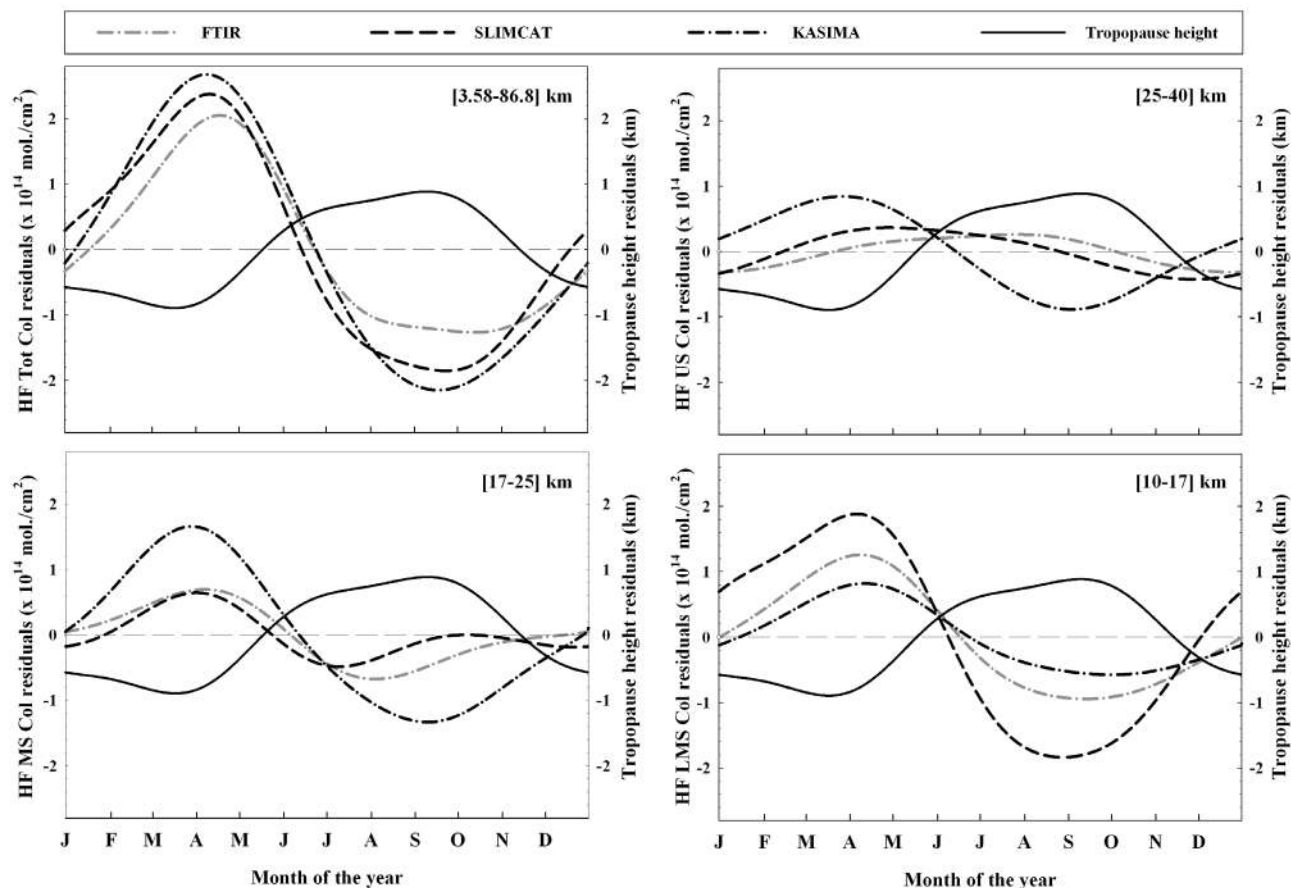
Figure 6. Dashed lines denote HF seasonal cycles derived from each time series in Figure 5. Solid line is tropopause height seasonal cycle as derived from NCEP p-T profiles computed for Jungfraujoch. The left vertical scale is valid for dashed lines. The right vertical scale is valid for the solid line.

HF seasonal cycle decreases with increasing altitude, suggesting that the HF variability is mainly controlled by dynamical effects that occur near the tropopause region. Among the few papers dealing with the HF seasonal cycle in the northern hemisphere, two separate studies by *Rinsland et al.* [1991, 2002] have exploited HF time series deduced from FTIR measurements performed at the U.S. National Solar Observatory facility on Kitt Peak (31.9°N, 111.6°W, 2090 m asl) to characterize its seasonal variation. In both papers, the HF seasonal cycle is modeled with a function that includes a sinusoidal component. The HF total column time series spanning the 1977–1990 time period has allowed *Rinsland et al.* [1991] to obtain a seasonal cycle that is characterized by an amplitude of close to 13% and with maximum HF vertical abundances at the end of March. These values have also been compared with simulations performed by the AER 2D model [*Ko et al.*, 1989] for 28.4°N latitude that provide an amplitude of 9% and maximum HF total columns around the beginning of July. In their subsequent paper, *Rinsland et al.* [2002] have performed a similar analysis of their HF stratospheric column amount time series (i.e., HF partial columns recovering the 14–50 km altitude range) above Kitt Peak between 1977 and 2001. Their investigations showed a seasonal amplitude of 10% and a maximum that occurs in mid March, which is quite consistent with their previous

results. The agreement between HF maxima found at Kitt Peak and at Jungfraujoch is good although the amplitude values differ substantially, probably as a direct consequence of the difference in latitude. This latter result is confirmed by examining an HF climatology at different latitudes, as exposed in Appendix A5.

[32] Among factors that influence the amplitude of the HF seasonal cycle, the annual variation of pressure and temperature definitely plays a role. Based on tests performed on our HF a priori profile, we have quantified the impact of such p-T variations on HF seasonal variability. These tests have revealed that the annual cycle characterizing p-T profiles generates variations on HF LMS, MS, US and total vertical abundances that do not excess 15%. Annual variations of pressure and temperature profiles above Jungfraujoch are consequently not able to fully explain the amplitude values reported in the last column of Table 5.

[33] As HF is a very stable gas with VMRs essentially constant and weak throughout the troposphere, one can imagine that the tropopause altitude could also influence both HF vertical amounts and its seasonal cycle, mainly in the altitude levels located near the tropopause (the tropopause altitude definition adopted here is the thermal definition provided by *WMO* [1957], i.e., the altitude above which a temperature gradient lower than 2°C/km is maintained for at least 2 km and located above the 500 hPa level). We have

Table 5. HF Main Seasonal Cycle Characteristics Associated With Figure 6

	Max[a]	Min[a]	Amplitude[b] ($\times 10^{14}$ mol/cm^2)	Amplitude[c] (%)
		LMS (10–17 km)		
FTIR	08 April	13 September	2.20	113.26 ± 27.96 [29.89]
SLIMCAT	06 April	28 August	3.72	59.59 ± 5.76 [4.52]
KASIMA	11 April	01 October	1.39	74.19 ± 5.00 [5.35]
		MS (17–25 km)		
FTIR	07 April	04 August	1.37	24.37 ± 1.64 [1.75]
SLIMCAT	01 April	09 July	1.13	14.16 ± 1.24 [0.97]
KASIMA	28 March	10 September	2.99	55.39 ± 5.11 [5.46]
		US (25–40 km)		
FTIR	27 July	27 December	0.58	11.21 ± 1.21 [1.29]
SLIMCAT	29 April	28 November	0.79	14.84 ± 1.01 [0.79]
KASIMA	27 March	03 September	1.73	26.45 ± 2.42 [2.59]
		Total (3.58–86.8 km)		
FTIR	17 April	13 October	3.32	29.94 ± 8.65 [6.79]
SLIMCAT	10 April	23 September	4.23	31.72 ± 11.77 [9.24]
KASIMA	08 April	17 September	4.83	42.86 ± 9.68 [7.59]

[a]For both FTIR and model data sets, Max and Min provide calendar dates for which HF maximum and minimum abundances, respectively, occur.
[b]Amplitude ($\times 10^{14}$ mol/cm^2) lists peak-to-peak amplitudes in vertical column units.
[c]Amplitude (%) gives corresponding amplitude values expressed in percent (see text for details). Values between brackets correspond to 2 times the standard error on the mean.

checked the validity of this hypothesis on the basis of tropopause heights deduced from NCEP temperature profiles computed for ISSJ. The use of NCEP data is justified by *Bizzarri et al.* [2006] who have demonstrated the good agreement that exists, for northern midlatitudes, between tropopause heights deduced from NCEP data and from satellite measurements. In addition, the comparison between NCEP and ECMWF temperature profiles above Bremen, Germany (located within 800 km of ISSJ) shows an agreement within 2K below 40 km (C. Vigouroux, personal communication, 2010). It is consequently reasonable to think that differences on tropopause heights derived from either of these data sets would be limited.

[34] The 1999–2009 tropopause height time series above ISSJ has been analyzed with the NPL statistical tool in order to derive its seasonal cycle. To make comparisons with FTIR and model data easier, the tropopause altitude seasonal cycle above Jungfraujoch has been reproduced with a black solid line on each panel of Figure 6. For this latter curve, we have computed a peak-to-peak amplitude that is equal to 1.78 km or, based on annual mean values, around 16%. One can also observe that the tropopause height peaks at its maximum (minimum) in March (September), so that HF and tropopause height seasonal cycles are out of phase for all altitude ranges, except for the US region (HF cycle as derived from KASIMA data is however out of phase with the tropopause height cycle for all regions). For these 3 regions, an anticorrelation between the tropopause height and HF amounts should exist, i.e., that high (low) tropopause heights should lead to low (high) HF VMR and vertical abundances. This is well illustrated in Figure 7, which reproduces HF profiles retrieved from 2 distinct FTIR spectra recorded at Jungfraujoch during February and October 1999. Corresponding tropopause heights are 8.7 km and 13.8 km (for comparison, the 1999–2009 mean tropopause altitude above Jungfraujoch is close to 11.3 km; see below) and are well representative of low and high tropopause height conditions (see next paragraph). The HF a priori profile used during our inversions and based on ACE-

FTS measurements (see section 2.1) is also reproduced with a dashed line. For both retrieved profiles, corresponding HF LMS, MS, US and total columns are given in the legend. As expected, the influence of the tropopause altitude both on retrieved HF profiles and vertical abundances is clear. Based on partial column values reported in boxes, the impact of the tropopause height on HF abundances seems however to be limited above 25 km.

[35] We have precisely quantified the impact of a change of tropopause height on HF partial and total vertical abundances. The mean tropopause height (for the 1999–2009 time period) above Jungfraujoch is close to 11.3 km (the corresponding 1 σ standard deviation equals 1.3 km). We have then selected all FTIR observations for which the corresponding tropopause height falls between 13.4 and 14.4 km (8.3 and 9.3 km), i.e., in an interval of 1 km width centered on the mean tropopause height value plus (minus) 2 σ standard deviations. The first (second) subset of FTIR data is consequently well representative of high (low) tropopause height conditions and will be denoted hereafter by HTC (LTC). These two subsets contain 166 (HTC) and 53 (LTC) individual FTIR spectra. A third subset, that contains all FTIR data for which the tropopause height lies between 10.8 and 11.8 km (i.e., in an interval of 1 km width, centered on the mean tropopause height value above Jungfraujoch) has been used as the reference (REF). This latter subset contains 738 individual FTIR observations. For each subset, we have computed mean HF LMS, MS, US and total columns. Comparison of mean HF column values obtained from HTC and REF subsets leads to the following relative differences (computed with respect to the REF subset, values are in percent) for LMS, MS, US and total columns: −55.2, −14.3, 3.0 and −13.3%, respectively. The same comparison performed for the LTC and REF subsets provides the following relative differences (for LMS, MS, US and total columns): 100.8, 5.5, 2.7 and 21.4%, respectively. It thus appears that high tropopause heights significantly reduce HF amounts (almost all relative differences reported are negative), in particular in the LMS region. A
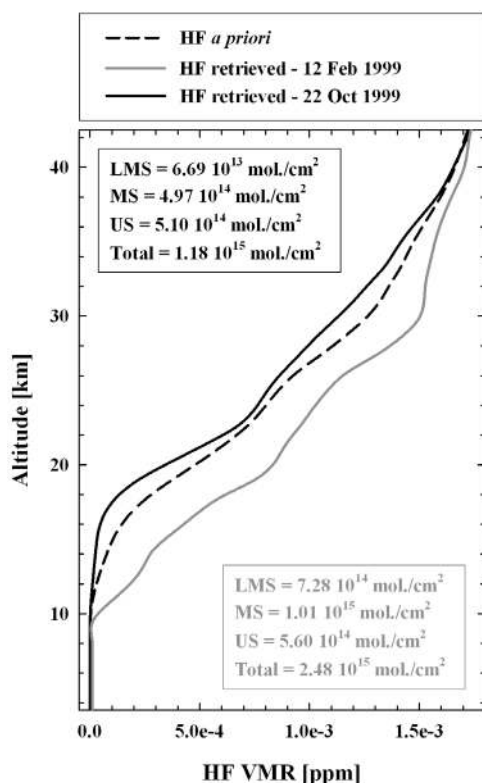
Figure 7. Typical example of individual HF retrieved profiles with PROFFIT 9.5 (black and gray solid lines) from two FTIR measurements at Jungfraujoch when different tropopause heights are observed (here, the tropopause height equals 8.7 km on 12 February 1999 and 13.8 km on 22 October 1999). The HF a priori profile used for our inversion is reproduced with the dashed line. For each retrieved profile, corresponding total and partial columns are given in separate boxes.

slight increase is however observed for the US region. Moreover, low tropopause height conditions significantly increase HF abundances, in particular LMS and total amounts. In both tropopause height conditions, MS and US abundances are less affected. The impact observed on HF total columns is mainly ascribable to the variations observed in the LMS region.

[36] Finally, to quantify the strength of the link that exists between HF partial or total column values and the tropopause height, we have evaluated correlation coefficients ρ between these parameters, by using the estimator

$$\rho = \frac{\sum (X_i - X_{mean}) \cdot (Y_i - Y_{mean})}{\sqrt{\sum (X_i - X_{mean})^2} \cdot \sqrt{\sum (Y_i - Y_{mean})^2}}. \quad (2)$$

Coefficient values obtained when considering FTIR or model HF data are reported in Table 6. As expected, the strongest and most significant anticorrelations are observed in the LMS range, which is the closest region to the tropopause and consequently, the most influenced by dynamical effects that alter the tropopause height. Except for the KASIMA data set, correlation coefficients are significantly reduced when moving from LMS to upper regions. More-

over, quite low variations observed for KASIMA correlation coefficients are in direct agreement with the permanent phase difference observed between KASIMA and tropopause height curves throughout each panel of Figure 6. Such behavior is probably ascribable to a slightly too strong Brewer-Dobson circulation in KASIMA simulations. That is further confirmed by Figure 11 of *Stiller et al.* [2008] that compares mean age of stratospheric air derived from KASIMA runs with those deduced from measurements of the Michelson Interferometer for Passive Atmospheric Sounding (MIPAS) [*Fischer et al.*, 2007]. In particular, *Stiller et al.*'s [2008] Figure 11 shows that, at midlatitudes, KASIMA gives slightly younger mean age of air in the lowermost and lower-middle parts of the stratosphere. Finally, comparison between correlation coefficient values found for HF LMS and total columns also seem to indicate that the seasonal cycle characterizing HF total column time series is mainly ascribable to seasonal variations affecting HF abundances in the lowermost part of the stratosphere.

4. Summary and Conclusions

[37] This paper describes the updated retrieval strategy adopted to derive HF abundances and vertical profiles from solar spectra recorded at the northern midlatitude ground-based station of the Jungfraujoch with two FTIR spectrometers (one homemade and one commercial Bruker 120 HR) between March 1984 and December 2009. Inversions are based on the HF R(1) absorption line and are performed with the PROFFIT 9.5 algorithm. As the SFIT 2 code is widely used within the FTIR community to retrieve vertical abundances of atmospheric gases, we have performed for the first time, a comparison between HF total columns retrieved with PROFFIT with those derived with SFIT 2. This comparison was based on 1 year of HF observations at Jungfraujoch (which corresponds to about 200 FTIR spectra) and indicates a non significant mean relative difference of less than 1%, in good agreement with previous studies by *Hase et al.* [2004] performed on other atmospheric species. As frequent negative retrieved VMRs profiles have been observed for interfering gases with both codes, our inversions are performed on a logarithmic vertical scale. In addition, the impact of the choice of the line shape model (Voigt or Galatry) adopted to simulate HF absorption lines for HF retrieved total columns and vertical profiles, on fitting quality and on error budget has also been quantified. While a small but significant difference close to 1% is observed for total columns, HF retrieved profiles are significantly smoother, mainly between 25 and 40 km, when a Galatry line shape model is adopted. Fitting residuals are also smaller with the Galatry model, with the mean relative

Table 6. Correlation Coefficients Between HF Partial/Total Columns Derived From FTIR Measurements or Model Runs and Corresponding Tropopause Heights[a]

	ρ_{FTIR}	$\rho_{SLIMCAT}$	ρ_{KASIMA}
LMS (10–17 km)	−0.57	−0.60	−0.50
MS (17–25 km)	−0.25	−0.13	−0.41
US (25–40 km)	0.10	0.02	−0.33
Total (3.58–86.8 km)	−0.44	−0.54	−0.43

[a]The number of data couples used in each computation is 1330.

Table A1. Main Characteristics of FTIR Spectra Analyzed in the Present Study

Spectrometer	Investigated Time Period	Filter range (cm^{-1})	Resolution (10^{-3} cm^{-1})	N[a]
Homemade	March 1984 to May 1984	2850–5350	12.74	9
Homemade	May 1984 to January 2008	3900–5150	8.01	676
Homemade	June 1984 to January 2008	2380–4400	9.69	407
Bruker-120 HR	January 1996 to December 2009	3900–4350	4.00	2471

[a]N is number of FTIR spectra that have been fitted in each wave number range.

difference between the approaches reaching almost 20%. Based on this, we have decided to include the Galatry line shape model in our retrieval approach.

[38] The vertical information content analysis has also indicated that, in addition to its total column, three independent HF partial columns could be derived from our Bruker spectra. They cover the lowermost part of the stratosphere (10–17 km, LMS), the lower-middle stratosphere (17–25 km, MS) and the middle-upper stratosphere (25–40 km, US). Due to poorer spectral resolution and signal-to-noise ratio, it is only possible to derive two HF partial columns (approximately extending between 10 and 20 km, and between 20 and 40 km) from our homemade observations. Our HF error budget estimates the contribution of seven different systematic or statistical error sources and clearly confirms that, with a contribution ranging from 5 to 6.5% depending on the altitude region under investigation, the main component of the total systematic error is the spectroscopy. The total systematic error characterizing our Bruker HF total columns equals 6%. The corresponding statistical error is close to 2%. For other altitude ranges, the total statistical error varies between 4.5 and 11.5%, and decreases with increasing altitude. The impact of the line shape model (Voigt or Galatry) on the error budget remains globally limited, the main issue being that the use of the Voigt model allows to significantly reduce by a few percent the total systematic error in the lower stratosphere. This benefit is however small compared to major improvements obtained (i.e., on global fit residuals and on HF vertical retrieved profiles) when a Galatry model is adopted and consequently, does not justify by itself the adoption of the Voigt model in our final retrieval strategy.

[39] We have also compared our Bruker HF MS and US vertical abundances with those derived from two satellite instruments (HALOE and ACE-FTS). For the two altitude ranges under consideration, no significant difference has been observed between FTIR and HALOE measurements. The agreement is better in the US region than in the MS range, in line with previous comparisons involving HALOE HF products. Moreover, we have noticed a small but significant bias between FTIR and ACE-FTS HF partial columns, with satellite measurements being higher than those deduced from our ground-based observations. However, this bias should be reduced in the forthcoming comparisons involving ACE-FTS version 3.0 products.

[40] Our daily mean FTIR HF total and partial columns have also been compared with those computed for Jungfraujoch by two numerical models (SLIMCAT and KASIMA). Comparisons for total columns cover the historical 1984–2009 time period and the 1996–2009 time period for the three partial columns. The agreement

between FTIR and KASIMA data is excellent below 25 km and for total columns while a significant bias close to 20% is observed in the US region. The contrary is observed when considering FTIR and SLIMCAT time series, as SLIMCAT runs seem to systematically overestimate total column HF abundances and the lower stratospheric contribution. For each of these data sets and for each altitude ranges, an analysis of the HF seasonal cycle has also been performed using a statistical tool based on a bootstrap resampling method. Except for the US region, we have found a strong seasonal variation, with the maximum observed in spring and the minimum in the second half of the year (between July and December). Peak-to-peak amplitudes characterizing FTIR and model HF total column seasonal cycles range from 30 to 40%. Comparison between HF abundances and tropopause height seasonal cycles indicates a strong phase difference. As expected, correlation coefficients computation between those two parameters suggests a good anticorrelation between HF LMS amounts and the tropopause height. Comparison between correlation coefficient found for HF total and LMS partial columns also suggests that the HF total column seasonal cycle is mainly ascribable to seasonal variations that occur in the lower stratosphere.

Appendix A

A1. Additional FTIR Database Statistics

[41] For the Bruker (homemade) spectrometer, our database includes 2471 (1092) FTIR spectra recorded over 1335 (301) sunny days. The spectral resolution (defined as the reciprocal of twice the maximum optical path difference) is equal to 4.10^{-3} cm^{-1} for the Bruker spectrometer. For the homemade instrument, three different optical filters have been used, leading to different spectral resolutions. More details for both instruments regarding the investigated time periods, corresponding spectral resolutions as well as additional statistics are given in Table A1.

A2. Retrieval Input Parameters

[42] Table A2 provides an overview of main retrieval input parameters adopted during our final HF retrieval strategy with the PROFFIT 9.5 algorithm.

A3. HF Information Content Analysis

[43] The vertical information contained in the FTIR spectra can be fully characterized by the averaging kernel matrix **A**, which can be calculated via the following expression [*Rodgers*, 2000]:

$$A = \left(K^T S_e^{-1} K + S_a^{-1}\right)^{-1} K^T S_e^{-1} K, \tag{A1}$$

Table A2. Main Regularization Parameters and Ancillary Inputs Adopted for our Final HF Inversions With PROFFIT 9.5

Parameter	Adopted Settings or Inputs
Microwindow limits	4038.81−4039.07 cm^{-1} (see Table 1)
Target gas	HF (VMR profile is fitted by OEM)
Interfering species	H_2O, HDO, CH_4 (VMR profiles are fitted with a TP regularization)
a priori HF VMR	Mean of all ACE-FTS v2.2 records in 41°N–51°N between 2004 and 2008 (see Figure 1, left)
a priori HF S_a	Based on all ACE-FTS v2.2 records in 41°N–51°N between 2004 and 2008 (see section 2.1)
HF spectroscopy	HITRAN 2004, Galatry line shape model assumed
p-T profiles	NCEP daily profiles specifically computed for ISSJ
Layering	41 layers (see background of Figure 1, left)

where S_a is the a priori covariance matrix (see section 2.1) and S_e the measurement error covariance matrix. The **K** matrix is the Jacobian of the forward model and indicates how much the FTIR measurements are sensitive to the parameters of the forward model adopted for the retrieval [*Rodgers*, 2000]. The averaging kernel matrix **A** depends on various experimental and retrieval parameters involved, such as the SZA, the spectral resolution, the spectral signal-to-noise ratio of the observation, the choice of microwindows, etc. Rows of **A** are the so-called averaging kernels (AvK) and characterize

the vertical range as well as the altitude resolution of the retrievals. Indeed, at a given altitude, full width at half maximum (FWHM) of AvK provides a measure of the vertical resolution of the retrieval. Thin gray curves in Figure A1 (left) reproduce typical (i.e., for a FTIR spectrum whose SZA is close to 55°, which corresponds to the mean SZA value found for our whole Bruker HF database) individual AvK for HF retrievals at ISSJ, i.e., AvK relative to each of the 41 atmospheric layers used in our forward model scheme. These curves indicate that our retrievals are most sensitive to HF between 10 and 40 km.

[44] The vertical information content of the retrieved target gas can also be quantified by the number of degrees of freedom for signal (DOFS), which is the sum of the appropriate trace section of the **A** matrix. The DOFS indicates the number of independent pieces of information that can be retrieved from the measurement. In our case, the mean DOFS (±1 σ standard deviation) computed over the whole Bruker time series equals 2.94 ± 0.24, meaning that three independent HF partial columns can be derived from our Bruker FTIR measurements. Hereafter, we will discuss the HF partial column amounts, defined in three independent atmospheric layers. The layer limits are chosen such that the DOFS reaches at least 1.0 inside the associated partial column. Following this approach, additional black curves in Figure A1 (left) reproduce merged AvK for the three atmospheric layers obtained and for which limits are
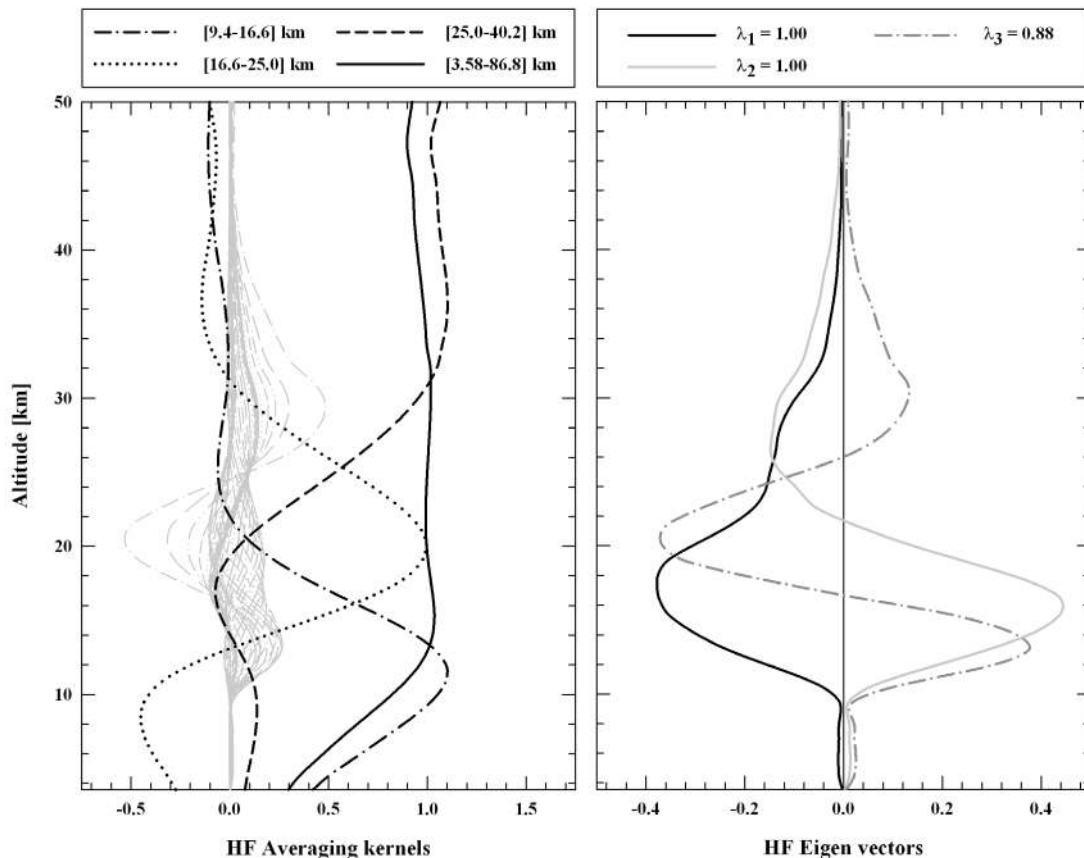

Figure A1. (left) Typical individual (thin gray curves) and merged (black curves) HF averaging kernels. For merged-layer kernels, corresponding atmospheric layers are specified in the legend. (right) Corresponding three first eigenvectors. Associated eigenvalues are given in the legend.

Table A3. Main Systematic and Statistical Errors (%) for HF Total and Partial Columns at Jungfraujoch[a]

	Total Column 3.58–86.8 km	LMS 10–17 km	MS 17–25 km	US 25–40 km
	Systematic Errors			
Spectroscopy	4.95 ± 0.02	6.49 ± 0.39	5.50 ± 0.20	6.56 ± 0.11
	4.96 ± 0.01	**5.97 ± 0.25**	**5.32 ± 0.24**	**6.46 ± 0.05**
Temperature profile[b]	0.20 ± 0.01	*1.57 ± 0.27*	0.67 ± 0.22	*0.68 ± 0.08*
	0.20 ± 0.01	***1.06 ± 0.10***	**0.82 ± 0.21**	***0.55 ± 0.04***
Solar parameters	0.02 ± 0.01	0.24 ± 0.16	0.03 ± 0.02	0.02 ± 0.01
	0.02 ± 0.01	**0.17 ± 0.12**	**0.04 ± 0.03**	**0.01 ± 0.01**
LOS	0.20 ± 0.15	0.22 ± 0.18	0.23 ± 0.17	0.26 ± 0.20
	0.20 ± 0.15	**0.22 ± 0.18**	**0.22 ± 0.17**	**0.26 ± 0.22**
ILS	0.59 ± 0.16	5.08 ± 1.31	3.00 ± 0.58	2.89 ± 0.35
	0.58 ± 0.11	**2.96 ± 0.86**	**3.22 ± 0.48**	**2.25 ± 0.33**
Baseline	0.06 ± 0.01	0.11 ± 0.05	0.03 ± 0.01	0.12 ± 0.05
	0.06 ± 0.01	**0.09 ± 0.02**	**0.03 ± 0.01**	**0.11 ± 0.04**
Total[b]	6.03 ± 0.32	*13.71 ± 1.54*	9.47 ± 0.58	10.54 ± 0.59
	6.03 ± 0.26	***10.47 ± 1.09***	**9.65 ± 0.35**	**9.64 ± 0.49**
	Statistical Errors			
Noise	0.47 ± 0.13	8.76 ± 3.63	2.97 ± 0.67	1.62 ± 0.45
	0.59 ± 0.14	**6.73 ± 2.41**	**3.90 ± 0.51**	**1.31 ± 0.41**
Temperature profile[b]	0.46 ± 0.03	3.66 ± 0.63	1.57 ± 0.52	*1.59 ± 0.18*
	0.47 ± 0.02	**2.47 ± 0.22**	**1.91 ± 0.49**	***1.29 ± 0.08***
Solar parameters	0.07 ± 0.03	0.98 ± 0.64	0.13 ± 0.07	0.06 ± 0.05
	0.07 ± 0.03	**0.70 ± 0.50**	**0.16 ± 0.11**	**0.04 ± 0.04**
LOS	1.84 ± 1.39	1.94 ± 1.59	2.00 ± 1.49	2.34 ± 1.80
	1.72 ± 1.50	**1.88 ± 1.67**	**1.85 ± 1.64**	**2.19 ± 1.89**
ILS	0.59 ± 0.16	5.08 ± 1.31	3.00 ± 0.58	2.89 ± 0.35
	0.58 ± 0.11	**2.96 ± 0.86**	**3.22 ± 0.48**	**2.25 ± 0.33**
Baseline	0.06 ± 0.01	0.11 ± 0.05	0.03 ± 0.01	0.12 ± 0.05
	0.06 ± 0.01	**0.09 ± 0.02**	**0.03 ± 0.01**	**0.11 ± 0.04**
Total	2.14 ± 1.26	11.43 ± 3.21	5.21 ± 0.71	4.58 ± 1.28
	2.13 ± 1.27	**8.37 ± 1.93**	**5.98 ± 0.59**	**3.92 ± 1.32**

[a]Values not boldfaced are for a Galatry line shape model, and boldfaced values are for a Voigt model. Errors given here are mean values computed over a sample of 5 FTIR spectra (see Table A4). Associated uncertainties are 2 times the standard error on the mean.

[b]Italicized values appear when a significant difference occurs between the line shape models.

defined in the legend (the black solid curve reproduces the AvK corresponding to the HF total column). One can see that these three layers are effectively independent, as their AvK peaks and are centered fairly closely on the middle of their corresponding layer limits. Based on the FWHM of AvK, the vertical resolution characterizing our HF retrieved profiles is close to 10 km. Due to poorer spectral resolution, the information content associated with our homemade spectra is lower and equals 2.40 ± 0.38 (mean DOFS value ±1 σ standard deviation computed over our entire home-made database), indicating that only two HF partial columns can be derived from our homemade FTIR spectra. Corresponding averaging kernel analysis has demonstrated that these two partial columns approximately extend between 10 and 20 km and between 20 and 40 km.

[45] To examine and quantify the influence of the a priori state on the retrieval, eigenvectors (and associated eigenvalues) of the **A** matrix can also be used [*Rodgers*, 1990, 2000]. Explicitly, while eigenvectors of **A** provide an indication concerning the sensitivity range, the associated eigenvalues give the fraction of information effectively coming from the measurement (the remaining information coming from the a priori). In other words, eigenvalues close to 1.0 represent components of the true profile which are well measured, while eigenvalues close to zero correspond to components which depend on the a priori state. Figure A1 (right) illustrates the three first eigenvectors of the **A** matrix

for which Avk are illustrated in Figure A1 (left). Associated eigenvalues (λ_i) are given in the legend. In particular, this plot shows that eigenvectors with a vertical structure broader (narrower) than the vertical resolution have less (more) dependence on the a priori. The sensitivity range deduced from this eigenvector plot is also in good agreement with the thin gray curves reproduced in Figure A1 (left). In addition, the third eigenvalue indicates that for the three HF partial columns defined, the fraction of information coming from the a priori is limited to around 10%.

A4. HF Total and Partial Columns Error Budget

[46] Systematic and statistical errors characterizing our HF total, LMS, MS and US columns have also been

Table A4. Main Characteristics of the FTIR Spectra Selected for Our HF Error Budget Evaluation

Spectra Name[a]	Date	SZA (deg)	SNR[b]
124159SA	13 Apr 1997	40.52	2853
121437SA	02 Aug 1999	29.92	3925
092943SA	30 Sep 2002	54.81	3143
115420SA	15 Dec 2005	70.16	3303
144815SA	15 Jan 2009	80.04	2084

[a]The name of each spectrum refers to the time (in UT hours, minutes, and seconds) of recording (two last characters denote the optical filter).
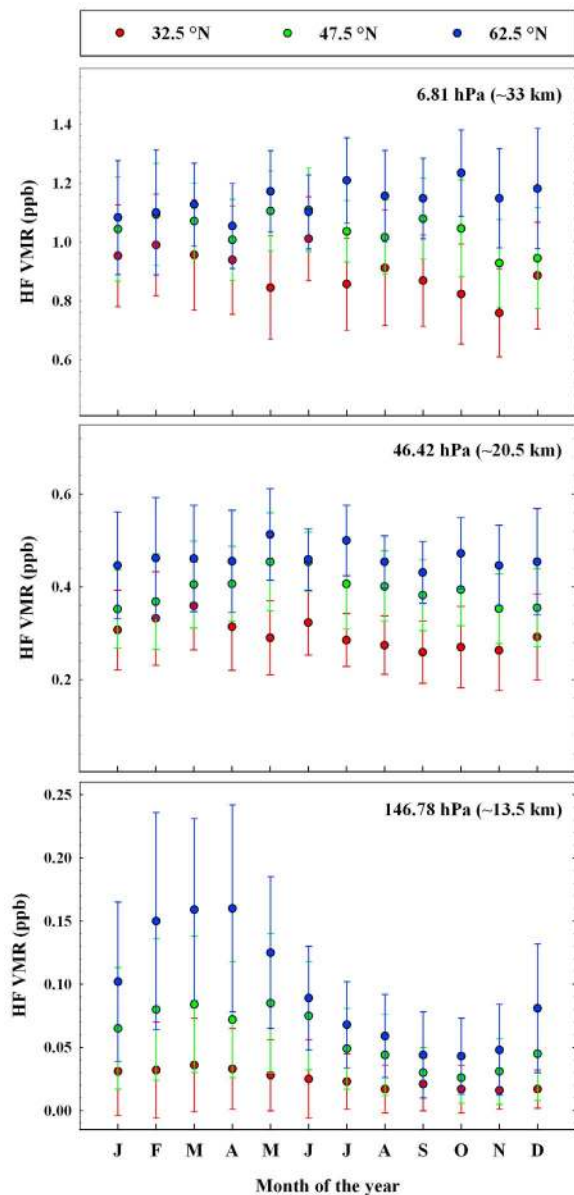
[b]Signal-to-noise ratio.

Figure A2. HF monthly mean concentrations derived from the HALOE climatology between years 1991 and 2002 at three different equivalent latitudes (see legend at top) and for three pressure levels (corresponding approximate altitudes are given between parentheses). Error bars are 1 σ standard deviation around the mean. Data are available as a supplement to *Grooß and Russell* [2005].

computed and are listed in Table A3 (in percent). These error values ΔC have been extracted from their associated VMR error covariance matrix **S** using the relation

$$\Delta C = \sqrt{\left(\frac{\partial C}{\partial VMR}\right)^{T} S \left(\frac{\partial C}{\partial VMR}\right)}, \qquad (A2)$$

where the derivative $\dfrac{\partial C}{\partial VMR}$ is the operator that transforms volume mixing ratio profiles into partial column quantities.

For a given partial column, it is a vector whose elements are set to zero outside the altitude range of the concerned column.

[47] In order to estimate the impact of the line shape profile on our HF error budget, Table A3 provides error values for both Galatry (normal font) and Voigt (bold font) line shape models. Again, error values provided in Table A3 are mean errors averaged over the 5 FTIR observations reported in Table A4. As we have used 5 FTIR spectra to compute the mean errors, we have decided to derive uncertainties characterizing these means by taking two times the standard error on the mean ($2 \times STE = 2 \times \sigma/\sqrt{N}$, where σ is the standard deviation around the mean and N the number of FTIR spectra involved, i.e., N = 5), in order to estimate the 95% confidence level. Apart from errors due to spectroscopy, spectral noise, temperature profile and ILS, it is clear from Table A3 that for all other error sources and for all altitude ranges reported, the choice of line shape model has very limited impact. For the errors due to spectroscopy, spectral noise and ILS, the main difference between both line shape models is observed in the lowermost stratosphere (LMS), where the Voigt model gives lower error values. These differences are however not significant, based on the uncertainties characterizing these errors. The spectroscopy remains the main source of systematic error. For all altitude ranges, we found values in the range 5 to 6.5%, which seems to be in good agreement with the 5% spectroscopic uncertainty value reported by *Rinsland et al.* [2002] for their stratospheric HF columns. The error estimation made by *Rinsland et al.* [2002] is however based on a 4% error for the HF lines intensity, instead of a 5% value assumed in the present study.

[48] The only significant difference between both the Galatry and Voigt models (at 95% confidence level) is observed for the systematic and statistical contributions associated to temperature profile error in the LMS and US regions, where the Voigt model reduces corresponding errors. These differences are probably ascribable to different dependences on temperature of the Voigt and Galatry models. As a consequence of the general improvement by the Voigt model in the LMS region, the total systematic error is significantly reduced by a few percent when adopting this line shape model. However, this benefit is small compared to the significant improvement observed in the fitting quality (close to 20%, see section 2.3) as well as other considerations based on Jungfraujoch spectra published by *Barret et al.* [2005] (i.e., smoother HF retrieved vertical profiles and better agreement with HALOE data), which altogether justify the adoption of the Galatry line shape model in our final HF retrieval strategy.

[49] Finally, the error budget computation from 5 typical homemade spectra has allowed us to check the good consistency that exists between systematic and statistical total errors affecting HF total columns derived from our two instruments. Indeed, these errors are in close agreement, within their respective uncertainties, with total error values reported in Table A3. Regarding systematic and statistical total errors affecting HF partial columns we could extract from our homemade spectra, they equal 9.91 ± 1.61% and 6.10 ± 1.68%, respectively, for the 10–20 km altitude range, and 8.24 ± 0.57% and 2.76 ± 0.62%, respectively, for the 20–40 km region. After comparison with Bruker error values obtained for the two same altitude ranges, it appears

that our homemade total errors are higher than our Bruker total errors by a factor ranging from 0.5 to 2.5%, typically. This can be explained by the fact that our Bruker spectra are characterized by higher spectral resolution and signal-to-noise ratio, as well as by a better zero absorption level.

A5. Latitudinal Effect on the HF Seasonal Cycle Based on HALOE Climatology

[50] In a recent publication, *Grooß and Russell* [2005] present the stratospheric climatology of six atmospheric gases (including HF) based on HALOE v19 measurements between 1991 and 2002, and compiled for 5° equivalent latitude belts from 82.5°N to 82.5°S. Our Figure A2 is based on the corresponding HF climatology (available as a supplement at http://www.atmos-chem-phys.net/5/2797/2005/acp-5-2797-2005-supplement.tar) and presents HF VMR monthly averages (and corresponding $1\,\sigma$ standard deviations) for three selected equivalent latitude zones (labeled with red, green and blue dots). The two first equivalent latitude regions (32.5°N and 47.5°N) are those that approximately correspond to Kitt Peak and Jungfraujoch locations, respectively. Results for a third equivalent latitude region (67.5°N) have also been plotted in Figure A2, in order to show the influence of increasing latitude on HF seasonal variation. In addition, each panel of Figure A2 corresponds to different pressure levels (corresponding approximate altitudes are given between parentheses, for information). These levels have been selected such that they fall in the middle of our three FTIR sensitivity regions (i.e., LMS, MS and US regions). Figure A2 (bottom) clearly highlights the strong influence of increasing latitude on the HF seasonal cycle amplitude, in good agreement with the Jungfraujoch–Kitt Peak comparison performed in the present study. For northern midlatitudes (green dots on Figure A2), the HALOE experiment has also observed HF maximum (minimum) abundances between March and May (between September and November), in very good agreement with values reported in Table 5 for the LMS region. In addition, middle and top frames of Figure A2 indicate that, for all latitudes, the amplitude of the HF seasonal cycle is significantly reduced for higher altitude levels, although HALOE does not see a seasonal signal above 30 km. This is reasonably in line with results derived from our FTIR and SLIMCAT time series (see gray dash-dotted and black dashed curves on Figure 6 and amplitude values reported in Table 5), even if FTIR and SLIMCAT data still display an amplitude of between 10 and 15% in the US region.

References

Barret, B., et al. (2005), Line narrowing effect on the retrieval of HF and HCl vertical profiles from ground-based FTIR measurements, *J. Quant. Spectrosc. Radiat. Transfer*, 95, 499–519.

Bernath, P. F., et al. (2005), Atmospheric Chemistry Experiment (ACE): Mission overview, *Geophys. Res. Lett.*, 32, L15S01, doi:10.1029/2005GL022386.

Bian, H., and M. J. Prather (2002), Fast-J2: Accurate simulation of stratospheric photolysis in global chemical models, *J. Atmos. Chem.*, 41, 281–296, doi:10.1023/A:1014980619462.

Bizzarri, B., et al. (2006), Analysis of seasonal and daily mid-latitude tropopause pressure using GPS radio occultation data and NCEP-NCAR reanalyses, in *Atmosphere and Climate Studies by Occultation Methods*, edited by U. Foelsche et al., pp. 253–263, Springer, Berlin.

Boone, C. D., et al. (2005), Retrievals for the atmospheric chemistry experiment Fourier-transform spectrometer, *Appl. Opt.*, 44, 7218–7231, doi:10.1364/AO.44.007218.

Chipperfield, M. P. (2006), New version of the TOMCAT/SLIMCAT offline chemical transport model: Intercomparison of stratospheric tracer experiments, *Q. J. R. Meteorol. Soc.*, 132, 1179–1203, doi:10.1256/qj.05.51.

Chipperfield, M. P., et al. (1997), On the use of HF as a reference for the comparison of stratospheric observations and models, *J. Geophys. Res.*, 102, 12,901–12,919, doi:10.1029/96JD03964.

Chou, S.-I., D. S. Baer, and R. K. Hanson (1999), Diode laser measurements of He-, Ar-, and N_2-broadened HF lineshapes in the first overtone band, *J. Mol. Spectrosc.*, 196, 70–76, doi:10.1006/jmsp.1999.7847.

Coffey, M. T., W. G. Mankin, and A. Goldman (1989), Airborne measurements of stratospheric constituents over Antarctica in the austral spring, 1987: 2. Halogen and nitrogen trace gases, *J. Geophys. Res.*, 94, 16,597–16,613, doi:10.1029/JD094iD14p16597.

Considine, G. D., L. E. Daver, E. E. Remsberg, and J. M. Russell III (1999), Analysis of near-global trends and variability in Halogen Occultation Experiment HF and HCl data in the middle atmosphere, *J. Geophys. Res.*, 104, 24,297–24,308, doi:10.1029/1999JD900497.

De Mazière, M., et al. (2005), The exploitation of ground-based Fourier transform infrared observations for the evaluation of tropospheric trends of greenhouse gases over Europe, *Environ. Sci.*, 2, 283–293, doi:10.1080/15693430500405179.

Dicke, R. (1953), The effect of collision upon the Doppler width of spectral lines, *Phys. Rev.*, 89, 472–473, doi:10.1103/PhysRev.89.472.

Duchatelet, P., et al. (2009), An approach to retrieve information on the carbonyl fluoride (COF_2) vertical distribution above Jungfraujoch by FTIR multi-spectrum multi-window fitting, *Atmos. Chem. Phys.*, 9, 9027–9042, doi:10.5194/acp-9-9027-2009.

Feng, W., et al. (2007), Mid-latitude ozone changes: Studies with a 3-D CTM forced by ERA-40 analyses, *Atmos. Chem. Phys.*, 7, 2357–2369, doi:10.5194/acp-7-2357-2007.

Fischer, H., et al. (2007), MIPAS: An instrument for atmospheric and climate research, *Atmos. Chem. Phys.*, 7, 8795–8893, doi:10.5194/acpd-7-8795-2007.

Fu, D., et al. (2009), First global observations of atmospheric COClF from the Atmospheric Chemistry Experiment mission, *J. Quant. Spectrosc. Radiat. Transfer*, 110, 974–985, doi:10.1016/j.jqsrt.2009.02.018.

Galatry, L. (1961), Simultaneous effect of Doppler and foreign gas broadening on spectral lines, *Phys. Rev.*, 122, 1218–1223, doi:10.1103/PhysRev.122.1218.

Gardiner, T., et al. (2008), Trend analysis of greenhouse gases over Europe measured by a network of ground-based remote FTIR instruments, *Atmos. Chem. Phys.*, 8, 6719–6727, doi:10.5194/acp-8-6719-2008.

Grooß, J.-U., and J. M. Russell (2005), Technical note: A stratospheric climatology for O_3, H_2O, CH_4, NO_x, HCl and HF derived from HALOE measurements, *Atmos. Chem. Phys.*, 5, 2797–2807, doi:10.5194/acp-5-2797-2005.

Gunson, M. R., et al. (1996), The Atmospheric Trace Molecule Spectroscopy (ATMOS) experiment: Deployment on the ATLAS Space Shuttle missions, *Geophys. Res. Lett.*, 23, 2333–2336, doi:10.1029/96GL01569.

Hase, F., T. Blumenstock, and C. Paton-Walsh (1999), Analysis of instrumental line shape of high-resolution FTIR-spectrometers using gas cell measurements and a new retrieval software, *Appl. Opt.*, 38, 3417–3422, doi:10.1364/AO.38.003417.

Hase, F., et al. (2004), Intercomparison of retrieval codes used for the analysis of high-resolution, ground-based FTIR measurements, *J. Quant. Spectrosc. Radiat. Transfer*, 87, 25–52, doi:10.1016/j.jqsrt.2003.12.008.

Ko, M. K. W., N. D. Sze, and D. K. Weisenstein (1989), The role of dynamical and chemical processes in determining the stratospheric

concentrations of ozone in one-dimensional and two-dimensional models, *J. Geophys. Res.*, *94*, 9889–9896, doi:10.1029/JD094iD07p09889.

Kouker, W., I. Langbein, T. Reddmann, and R. Ruhnke (1999), The Karlsruhe Simulation Model of the Middle Atmosphere (KASIMA), version 2, *FZK Rep. 6278*, Forsch. Karlsruhe, Karlsruhe, Germany.

Mahieu, E., et al. (2008), Validation of ACE-FTS v2.2 measurements of HCl, HF, CCl_3F and CCl_2F_2 using space-, balloon- and ground-based instrument observations, *Atmos. Chem. Phys.*, *8*, 6199–6221, doi:10.5194/acp-8-6199-2008.

Mélen, F., et al. (1998), Vertical column abundances of COF_2 above the Jungfraujoch Station, derived from ground-based infrared solar observations, *J. Atmos. Chem.*, *29*, 119–134, doi:10.1023/A:1005847829686.

Monge-Sanz, B., M. P. Chipperfield, A. Simmons, and S. Uppala (2007), Mean age of air transport in a CTM: Comparison of different ECMWF analyses, *Geophys. Res. Lett.*, *34*, L04801, doi:10.1029/2006GL028515.

Montzka, S. A., et al. (1999), Present and future trends in the atmospheric burden of ozone-depleting halogens, *Nature*, *398*, 690–694, doi:10.1038/19499.

Nassar, R., P. F. Bernath, C. D. Boone, S. D. McLeod, R. Skelton, K. A. Walker, C. P. Rinsland, and P. Duchatelet (2006), A global inventory of stratospheric fluorine in 2004 on Atmospheric Chemistry Experiment Fourier transform spectrometer (ACE-FTS) measurements, *J. Geophys. Res.*, *111*, D22313, doi:10.1029/2006JD007395.

Notholt, J., A. Meier, and S. Peil (1995), Total column densities of tropospheric and stratospheric trace gases in the undisturbed arctic summer atmosphere, *J. Atmos. Chem.*, *20*, 311–332, doi:10.1007/BF00694500.

O'Doherty, S., et al. (2004), Rapid growth of HFC-134a, HCFC-141b, HCFC-142b and HCFC-22 from AGAGE observations at Cape Grim, Tasmania and Mace Head, Ireland, *J. Geophys. Res.*, *109*, D06310, doi:10.1029/2003JD004277.

Phillips, D. (1962), A technique for the numerical solution of certain integral equations of the first kind, *J. ACM*, *9*, 84–97.

Pine, A. S., and R. Ciurylo (2001), Multispectrum fits of Ar-broadened HF with a generalized asymmetric lineshape: Effects of correlation, hardness, speed dependence, and collision duration, *J. Mol. Spectrosc.*, *208*, 180–187, doi:10.1006/jmsp.2001.8375.

Pine, A. S., A. Freid, and J. W. Elkins (1985), Spectral intensities in the fundamental bands of HF and HCl, *J. Mol. Spectrosc.*, *109*, 30–45, doi:10.1016/0022-2852(85)90049-9.

Rautian, S. G., and I. I. Sobel'man (1967), The effect of collisions on the Doppler broadening of spectral lines, *Sov. Phys. Usp., Engl. Transl.*, *9*, 701–716, doi:10.1070/PU1967v009n05ABEH003212.

Reddmann, T., R. Ruhnke, and W. Kouker (2001), Three-dimensional model simulations of SF_6 with mesospheric chemistry, *J. Geophys. Res.*, *106*, 14,525–14,537, doi:10.1029/2000JD900700.

Reisinger, A. R., N. B. Jones, W. A. Matthews, and C. P. Rinsland (1994), Southern Hemisphere ground based measurements of carbonyl fluoride (COF_2) and hydrogen fluoride (HF): Partitioning between fluoride reservoir species, *Geophys. Res. Lett.*, *21*, 797–800, doi:10.1029/94GL00693.

Rinsland, C. P., J. S. Levine, A. Goldman, N. D. Sze, M. K. W. Ko, and D. W. Johnson (1991), Infrared measurements of HF and HCl total column abundances above Kitt Peak, 1997–1990: Seasonal cycles, long-term increases and comparisons with model calculations, *J. Geophys. Res.*, *96*, 15,523–15,540, doi:10.1029/91JD01249.

Rinsland, C. P., et al. (1998), Northern and Southern Hemisphere ground-based infrared measurements of tropospheric carbon monoxide and ethane, *J. Geophys. Res.*, *103*, 28,197–28,217, doi:10.1029/98JD02515.

Rinsland, C. P., et al. (2002), Stratospheric HF column abundances above Kitt Peak (31.9°N latitude): Trends from 1977 to 2001 and correlations with stratospheric HCl columns, *J. Quant. Spectrosc. Radiat. Transfer*, *74*, 205–216, doi:10.1016/S0022-4073(01)00233-3.

Rodgers, C. D. (1990), Characterization and error analysis of profiles retrieved from remote sounding instruments, *J. Geophys. Res.*, *95*, 5587–5595, doi:10.1029/JD095iD05p05587.

Rodgers, C. D. (2000), Inverse methods for atmospheric sounding: Theory and Practice, *Atmos. Oceanic Planet. Phys.*, vol. 2, World Sci., Hackensack, N. J.

Rothman, L. S., et al. (2005), The HITRAN 2004 molecular spectroscopic database, *J. Quant. Spectrosc. Radiat. Transfer*, *96*, 139–204, doi:10.1016/j.jqsrt.2004.10.008.

Ruhnke, R., W. Kouker, and T. Reddmann (1999), The influence of the OH + NO_2 +M reaction on the NO_y partitioning in the late Arctic winter 1992/1993 as studied with KASIMA, *J. Geophys. Res.*, *104*, 3755–3772, doi:10.1029/1998JD100062.

Russell, J. M., III, L. L. Gordley, J. H. Park, S. R. Drayson, W. D. Hesketh, R. J. Cicerone, A. F. Tuck, J. E. Frederick, J. E. Harries, and P. J. Crutzen (1993), The Halogen Occultation Experiment, *J. Geophys. Res.*, *98*, 10,777–10,797, doi:10.1029/93JD00799.

Russell, J. M., III, et al. (1996), Validation of hydrogen fluoride measurements made by the HALOE experiment from the UARS platform, *J. Geophys. Res.*, *101*, 10,163–10,174, doi:10.1029/95JD01705.

Sander, S. P., et al. (2003), Chemical kinetics and photochemical data for use in atmospheric studies: Evaluation number 14, *JPL Publ., 02–25*, 334 pp.

Sen, B., G. C. Toon, J.-F. Blavier, E. L. Fleming, and C. H. Jackman (1996), Balloon-borne observations of midlatitude fluorine abundance, *J. Geophys. Res.*, *101*, 9045–9054, doi:10.1029/96JD00227.

Senten, C., et al. (2008), Technical Note: New ground-based FTIR measurements at Ile de La Réunion: Observations, error analysis, and comparisons with independent data, *Atmos. Chem. Phys.*, *8*, 3483–3508, doi:10.5194/acp-8-3483-2008.

Stiller, G. P., et al. (2008), Global distribution of mean age of stratospheric air from MIPAS SF_6 measurements, *Atmos. Chem. Phys.*, *8*, 677–695, doi:10.5194/acp-8-677-2008.

Stolarski, R. S., and R. D. Rundel (1975), Fluorine photochemistry in the stratosphere, *Geophys. Res. Lett.*, *2*, 443–444, doi:10.1029/GL002i010p00443.

Tikhonov, A. (1963), On the solution of incorrectly stated problems and a method of regularization, *Dokl. Akad. Nauk SSSR*, *151*, 501-504.

Toon, G. C., C. B. Farmer, P. W. Schaper, L. L. Lowes, and R. H. Norton (1992), Composition measurements of the 1989 Arctic winter stratosphere by airborne infrared solar absorption spectroscopy, *J. Geophys. Res.*, *97*, 7939–7961, doi:10.1029/91JD03114.

Wilson, S. R., G. Schuster, and G. Helas (1989), Measurements of COFCl and CCl_2O near the tropopause, in Ozone in the Atmosphere, edited by R. D. Bojkov and P. Fabian, pp. 302–305, A. Deepak, Hampton, Va.

Wittke, J., and R. Dicke (1956), Redetermination of the hyperfine splitting in the ground state of atomic hydrogen, *Phys. Rev.*, *103*, 620–631, doi:10.1103/PhysRev.103.620.

World Meteorological Organization (WMO) (1957), Definition of the tropopause, *WMO Bull.*, *6*, 136.

World Meteorological Organization (WMO) (2007), Scientific Assessment of Ozone Depletion: 2006, *WMO Rep. 50*, Geneva, Switzerland.

Zander, R. (1975), Présence de HF dans la stratosphère supérieure, *C.R. Acad. Sci., Ser. B.*, *281*, 213–214.

Zander, R., et al. (1987), Monitoring of the integrated column of hydrogen fluoride above the Jungfraujoch Station since 1977: The HF/HCl column ratio, *J. Atmos. Chem.*, *5*, 385–394, doi:10.1007/BF00113901.

Zander, R., et al. (1992), The 1985 chlorine and fluorine inventories in the stratosphere based on ATMOS observations at 30° north latitude, *J. Atmos. Chem.*, *15*, 171–186, doi:10.1007/BF00053758.

Zander, R., P. Rinsland, E. Mahieu, M. R. Gunson, C. B. Farmer, M. C. Abrams, and M. K. W. Ko (1994), Increase of carbonyl fluoride (COF_2) in the stratosphere and its contribution to the 1992 budget of inorganic fluorine in the upper stratosphere, *J. Geophys. Res.*, *99*, 16,737–16,743, doi:10.1029/94JD01029.

P. F. Bernath, Department of Chemistry, University of York, York YO10 5DD, UK. (pfb500@york.ac.uk)

C. D. Boone and K. A. Walker, Department of Chemistry, University of Waterloo, Waterloo, ON N2L 3G1, Canada. (cboone@acebox.uwaterloo.ca; kwalker@atmosp.physics.utoronto.ca)

M. P. Chipperfield and W. Feng, Institute for Climate and Atmospheric Science, School of Earth and Environment, University of Leeds, Leeds LS2 9JT, UK. (martyn@env.leeds.ac.uk; w.feng@see.leeds.ac.uk)

P. Demoulin, P. Duchatelet, and E. Mahieu, Institute of Astrophysics and Geophysics of the University of Liège, Allée du 6 Août, 17, B-4000 Liège, Belgium. (demoulin@astro.ulg.ac.be; p.duchatelet@ulg.ac.be; emmanuel.mahieu@ulg.ac.be)

F. Hase and R. Ruhnke, Institute for Meteorology and Climate Research, Karlsruhe Institute of Technology, PO Box 3640, D-76021 Karlsruhe, Germany. (frank.hase@kit.edu; roland.ruhnke@kit.edu)